JGR Oceans

Influence of the Gulf of Guinea Islands on the Atlantic Equatorial Undercurrent Circulation

D. C. Napolitano[1,2] , **G. Alory[1]** , **I. Dadou[1]**, **Y. Morel[1]** , **J. Jouanno[1]** , and **G. Morvan[1]**

[1]Laboratoire d'Etudes en Géophysique et Océanographie Spatiales (LEGOS), Université de Toulouse, CNES, CNRS, IRD, UT3, Toulouse, France, [2]Now at CNRS, Ifremer, IRD, Laboratoire d'Océanographie Physique et Spatiale (LOPS), IUEM, University Brest, Plouzané, France

Abstract In the easternmost portion of the Gulf of Guinea, Bioko Island marks the beginning of an island chain that stretches NE–SW to the Equator, where São Tomé Island sits in the path of the Equatorial Undercurrent (EUC). In this study, we explore the meso-to-large-scale effects of local flow-topography interactions that escalate from the EUC encounter with the Gulf of Guinea islands. A mean shipboard Acoustic Doppler Current Profiler section captures the EUC as a strong subsurface jet that ultimately hits São Tomé. Motivated by these observations, we ran two ocean general circulation model simulations that differ by the presence versus absence of the Gulf of Guinea islands. Diagnostics of salinity and potential vorticity (PV) from these simulations show that the EUC bifurcates at 6°E, triggering mesoscale activity that spreads the EUC waters. On both sides of São Tomé, the EUC branches roll up into eddies that propagate westward. These low-PV anticyclones carry high salinity through the tropical Atlantic, introducing PV anomalies along eddy corridors mirrored by the Equator. The formation of such eddies is affected by diapycnal and isopycnal mixing and friction, and their distribution between hemispheres is intrinsically related to the location of São Tomé. The eddies are modulated at both seasonal and interannual scales. A strong EUC generates numerous and stronger eddies, while seasonal equatorial upwelling indirectly hinders their formation. Convergence of the EUC upstream of São Tomé reveals intense downwelling and freshening, whereas divergence and upwelling are associated with the EUC negotiating the island.

Plain Language Summary In the eastern portion of the tropical Atlantic, in the Gulf of Guinea, Bioko Island marks the beginning of an island chain that stretches NE–SW to the Equator, where São Tomé Island sits in the path of the strongest current in the tropical Atlantic, the Equatorial Undercurrent (EUC). The EUC connects the tropical Atlantic, transporting high-salinity waters eastward. In this study we explore the effects of flow-topography interactions on the EUC circulation. Velocity observations capture the EUC as a strong current that hits São Tomé Island. Motivated by these observations, we ran two model simulations that differ by the presence versus absence of the Gulf of Guinea islands. Diagnostics of salinity and potential vorticity (a dynamical quantity that relates to the circulation) show that the EUC bifurcates at 6°E, spreading the EUC waters. On both sides of São Tomé Island, the EUC branches form eddies that propagate westward through the tropical Atlantic. The formation and distribution of such eddies present an asymmetry between hemispheres due to the EUC interaction with São Tomé. On regional scales, a particle-tracking experiment reveals sinking before the particles reach São Tomé, with mixing and freshening of the EUC waters as they flow around the island.

1. Introduction

The Equatorial Undercurrent (henceforth EUC) is the strongest zonal current in the tropical Atlantic, dominating its large-scale circulation and intrabasin exchange. This current originates from one of the multiple North Brazil Current retroflections (e.g., Goes et al., 2005; Schott et al., 1998; Silveira et al., 2000), and contributes to the cross-equatorial salt and heat transport and subtropical-cell circulation which impacts the Atlantic Meridional Overturning Circulation (AMOC; e.g., Chang et al., 2008; Hazeleger et al., 2003; Rabe et al., 2008), transporting eastward mainly the saline and oxygen-rich Salinity Maximum Water (SMW; $T > 24°C$, $S > 37$) and South Atlantic Central Water (SACW; $T > 13°C$, $S > 35$) subducted in the subtropics (e.g., Blanke et al., 2002; Mémery et al., 2000; Snowden & Molinari, 2003; Stramma & Schott, 1999) to surface in the central and eastern equatorial Atlantic (e.g., Jouanno, Marin, Du Penhoat, Molines, & Sheinbaum, 2011; Jouanno, Marin, Du Penhoat, Sheinbaum, & Molines, 2011). Taken as the Atlantic counterpart of the previously studied Pacific EUC,

the structure of the Atlantic EUC was described by Metcalf et al. (1962) from sections of temperature, salinity, oxygen, and direct measurements of velocity and current shear. More recent studies improved the observational spatio-temporal resolution in the region, with Conductivity-Temperature-Depth (CTD), Acoustic Doppler Current Profiler (ADCP), and current mooring observations (e.g., Brandt et al., 2006; Johns et al., 2014; Kolodziejczyk et al., 2009) to understand the EUC structure and variability. In the present paper, we use a numerical model with improved bathymetry resolution to focus on a question which has not received particular attention: the impact of the Gulf of Guinea islands on the circulation of the EUC.

The EUC flows eastward at >0.4 m s^{-1} along the Equator, with reports of >0.7 m s^{-1} close to the center of the basin (23°W; Brandt et al., 2006). The current transport progressively decreases eastward, from ∼14 Sv at 23°W (Brandt et al., 2014; Johns et al., 2014) to ∼12 Sv at 10°W (Johns et al., 2014; Kolodziejczyk et al., 2009), ∼10.5 Sv at 0° (Johns et al., 2014; Kolodziejczyk et al., 2014), and ∼4 Sv at 6°E (Kolodziejczyk et al., 2014). These transports present variability at intraseasonal (Brandt et al., 2006; Jouanno et al., 2013), semiannual (Brandt et al., 2006; Johns et al., 2014), and interannual (Brandt et al., 2021) time scales, captured by both modeling and observational efforts, which continue to improve under the umbrella of projects such as PIRATA (Prediction Research Moored Array in the Tropical Atlantic; Bourlès et al., 2008; Bourlès et al., 2019), AtlantOS (Optimizing and Enhancing the Integrated Atlantic Ocean Observing Systems; https://www.atlantos-h2020.eu/), TAOS (The Tropical Atlantic Observing System; Foltz et al., 2019), and TRIATLAS (Tropical and South Atlantic Climate-Based Marine Ecosystem Prediction for Sustainable Management; https://triatlas.w.uib.no/) among others.

In the eastern Gulf of Guinea, the EUC approaches the region near 6°E, where the maximum salinity associated with the EUC bifurcates and westward return flows appear north and south of the Equator (e.g., Kolodziejczyk et al., 2014). Although the source waters and the retroflections at the origin of the EUC have been extensively studied (e.g., Blanke et al., 2002; Goes et al., 2005; Mémery et al., 2000; Schott et al., 1998; Silveira et al., 2000; Snowden & Molinari, 2003; Stramma & Schott, 1999, and others), little is known about its bifurcation on the eastern basin and the formation of the returning westward flows (e.g., Assene et al., 2020; Gouriou & Reverdin, 1992; Kolodziejczyk et al., 2014). Using observations and a 1/12° numerical simulation, Kolodziejczyk et al. (2014) described the seasonal cycle and bifurcation of the EUC between 5°E and the African continent, a region termed "termination site" by the authors. They showed a robust EUC seasonal cycle, with characteristic high-salinity waters present in the westward recirculations opposing the EUC in late boreal spring. Toward the end of summer, the EUC weakened and saline waters were not observed within the inner portions of the gulf. More recently, Assene et al. (2020) noted that the extra-equatorial westward return flows opposing the EUC were in fact associated with the mesoscale dynamics of the EUC. Using a 2 1/2-layer model, McCreary and Yu (1992) showed that an EUC-like jet is inherently unstable and shed anticyclonic eddies in both hemispheres. According to Assene et al. (2020), these successive mesoscale eddies that propagate westward spread their potential vorticity (PV) content to create zonal bands of nearly homogeneous PV. The eddies originate through the inverse energy cascade by the merging of small-scale PV anomalies, which were tracked back to the easternmost portions of the Gulf of Guinea (Assene et al., 2020) in a region populated by islands.

Flow-island interactions are known to generate mesoscale eddies in different regions of the ocean (e.g., Arístegui et al., 1994; Sangrà et al., 2009; Tchamabi et al., 2017). In the eastern Gulf of Guinea, several islands align to form a NE–SW oriented island chain. The three main islands, from the coastal to the open ocean—Bioko (3.5°N, 8.7°E), Príncipe (1.6°N, 7.4°E), and São Tomé (0.2°N, 6.6°E)—stand in the path of ocean currents, with flow-island interactions likely to affect the regional and larger-scale circulation. The southernmost of the three islands, São Tomé, is equivalent to the renowned Galápagos Islands (0.5°S, 91°W) in the Pacific, which have been shown to strongly interact with the Pacific EUC. Karnauskas et al. (2007) showed that the obstruction of the Pacific EUC by the Galápagos can significantly alter the circulation. Its bifurcation leads to main branches that continue flowing eastward and join the continental slope, preferentially to the south (e.g., Karnauskas et al., 2007; Montes et al., 2010), and to a partial return of the flow westward (e.g., Johnson et al., 2002; Karnauskas et al., 2007). Comparing simulations with and without the Galápagos islands at different resolution, Karnauskas et al. (2007) showed that flow-island interactions lead to a deeper thermocline, which yield positive SST anomalies and reduce the westward bias of the Pacific cold tongue, increasing sea surface temperature and ocean-atmosphere fluxes. Such effects even influence the periodicity of the El Niño Southern Oscillation (Karnauskas et al., 2008). Finally, the authors stated that major changes are produced when the islands are implemented at sufficient resolution on the model grid, otherwise even a strong flow such as the EUC would

only "glance" the islands (Karnauskas et al., 2007). This seems to be particularly the case for Kolodziejczyk et al. (2014)'s simulation, which, despite having sufficient horizontal resolution, fails to adequately resolve the islands in the Gulf of Guinea. In Kolodziejczyk et al. (2014), one cannot clearly see these islands, and the EUC bypasses them to bifurcate at the African continent.

In a theoretical study, Pedlosky and Spall (2015) used a shallow water model to represent the Pacific EUC interaction with Galápagos. For a "supercritical flow" as the EUC, the current is affected locally by the island, with no standing Rossby wave field. Their numerical solutions showed the formation of dipole-like PV anomalies on the lee of the islands, which were also affected by placing the island asymmetrically from the Equator (for this case, the authors displayed only the subcritical flow). With a proper representation of islands, the *mise en scène* in the Gulf of Guinea suggests that similar consequences could arise from the interaction between islands and currents, particularly due to the obstruction of the EUC's strong zonal jet by São Tomé Island. In Kolodziejczyk's et al. (2014) configuration, the dynamics associated with the islands were not well captured. Later, Assene et al. (2020) suggested that mixing and frictional processes acting near the islands could play a role in the dynamics of the EUC and return flows.

Downscaling from the mean tropical Atlantic circulation into the eastern Gulf of Guinea, the primary objective of this study is to assess the impact of the Gulf of Guinea islands on the meso-to-large-scale circulation of the EUC. We confirm from regional observations that the EUC hits São Tomé, and then discuss the repercussions of this interaction using a numerical simulation focusing on how flow patterns and tracer transport are affected by the EUC interaction with the islands. Throughout the paper, we ask: (a) do the islands impact the bifurcation of the EUC?; (b) can this interaction have consequences for the return flows and the net fluxes across the Tropical Atlantic, especially through mesoscale dynamics?; and (c) how do regional processes near the islands impact the EUC dynamics?

2. Observational Motivation and the Numerical Approach

2.1. Tropical Atlantic Observations

To address the Gulf of Guinea islands' topography effects on the EUC circulation, we first identified the EUC along the Equator and west of São Tomé Island, from zonal velocity (u) and salinity observations. We used shipboard ADCP sections (Bourlès et al., 2018) at 6°E from five cruises—PIRATA Fr22, and EGEE 1, 2, 3, and 5 (processing details in Herbert et al., 2015, individual cruises in Supporting Information S1)—and salinity measurements derived from a moored CTD at (0°N, 0°E) between 2007 and 2017, part of the PIRATA buoy array. (No velocity data is available for this particular buoy). From each cruise track, we selected all ADCP velocity measurements between 2°S and 2°N, in a 0.1° box around 6°E. Continuous direct velocity measurements at the EUC are scarce in the region, and we acknowledge that the five cruises may not provide season-independent measurements for an ideal mean scenario (three cruises occur between May–July, one in April, and one in September). Nevertheless, the cruises capture the variability of the EUC in terms of strength, core depth, and latitudinal migration, showing particularly a stronger flow in EGEE2, EGEE5, and Fr22 and a weaker EUC in EGEE1 and EGEE3. We created a mean state of the zonal component of the EUC by merging the short time average (2 min) zonal velocity u from the cruises via objective mapping, with correlation lengths three times the processed data sampling interval, $\Delta x = 0.20°$ and $\Delta z = 15$ m in the horizontal and vertical directions, respectively, which are sufficient to resolve the EUC mesoscale dynamics of about 1° in the region. For the salinity, we used the moored CTD data available within the Enhanced PIRATA data set, a product with additional quality control, no temporal gaps, and vertically mapped to a 5-m grid (cf. Foltz et al., 2018).

Briefly, the analyzed datasets capture the EUC as a strong subsurface-intensified jet flowing eastward at the Equator at 6°E, hammering São Tomé Island about 50 km downstream (Figure 1a). Motivated by these EUC observations, we ran two numerical simulations of the NEMO model (Nucleus for European Modeling of the Ocean; Madec & the NEMO team, 2016), one reference simulation—hereafter NEMO With Islands (WI)—and another without the topography of the islands of the Gulf of Guinea, the NEMO No Islands (NI).

2.2. NEMO Simulations

The reference simulation is an eddy-resolving configuration of the equatorial and tropical Atlantic (20°S–20°N, 60°W–15°E) with 1/12° horizontal resolution and 75 vertical levels, nested in a 1/4° resolution
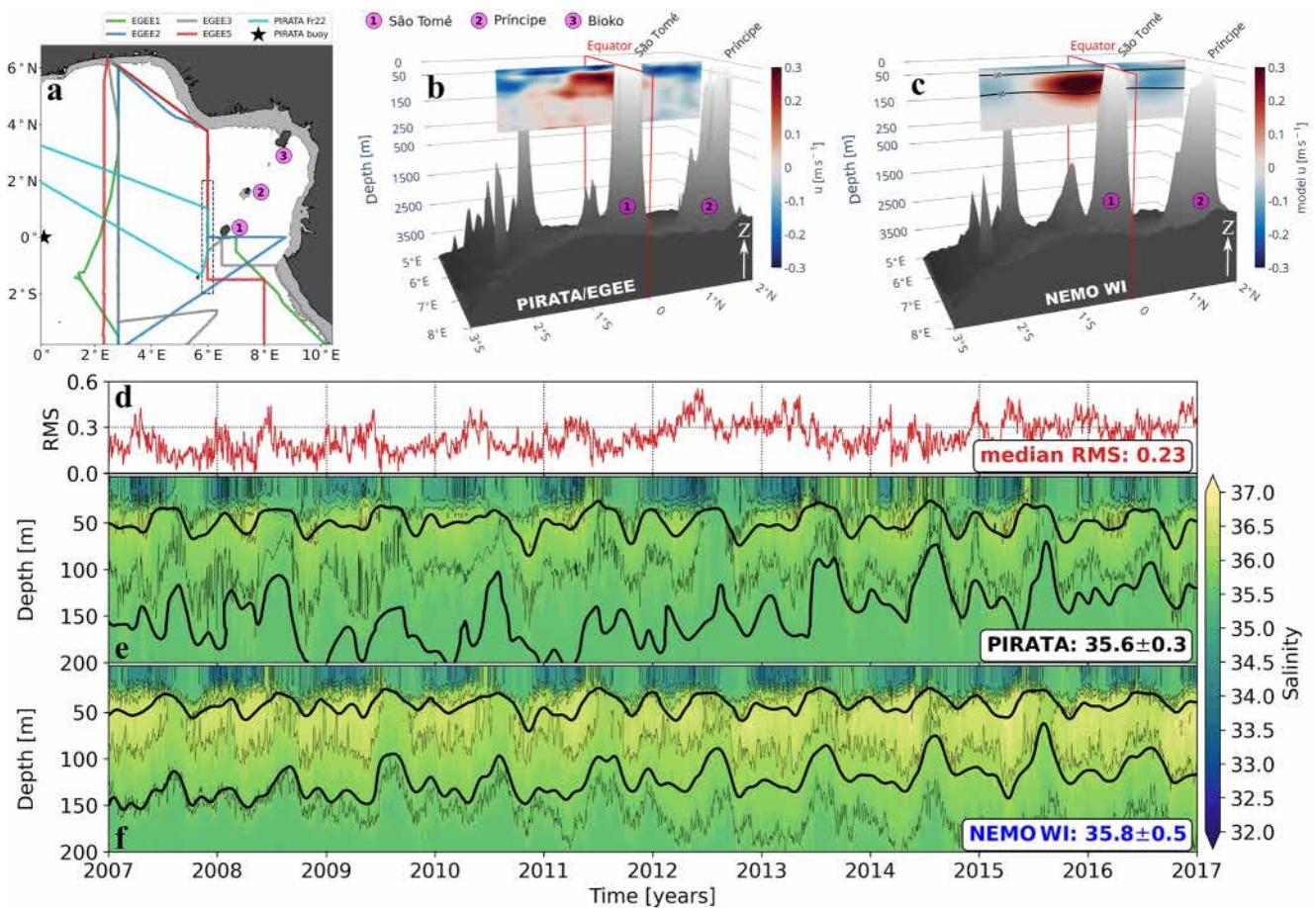
Figure 1. Comparison between observations and the Nucleus for European Modeling of the Ocean (NEMO) reference (WI) numerical simulation. (a) Map of the study region showing the location of the Gulf of Guinea islands (circles labeled 1–3), the five cruise tracks—Prediction Research Moored Array in the Tropical Atlantic (PIRATA) Fr22 (April 2012), EGEE 1 (June 2005), 2 (September 2005), 3 (June 2006), and 5 (June 2007)—and the moored buoy location (★). The dashed box shows the area sampled for the Acoustic Doppler Current Profiler (ADCP) vertical sections. (b) Objectively mapped mean zonal velocity (positive eastward) from shipboard ADCP data at 6°E. The vertical axis is rescaled for the upper 500 m. (c) NEMO 10-year-averaged vertical section of zonal velocity at 6°E; black lines represent the 36 salinity contour. (d) Root-mean-squared difference series between daily vertical profiles of salinity at (0°N, 0°E), comparing (e) the enhanced PIRATA data set buoy measurements with (f) the model series interpolated into the buoy vertical levels at the same location. In (e) and (f), thick black lines represent the 30-day filtered 1,025.3–1,026.4 kg m⁻³ density contours. The values in the horizontal axis of (f) indicate the beginning of each year of simulation.

eddy-permitting parent grid. The two domains are coupled online via the AGRIF library in two-way mode (Blayo & Debreu, 1999). We enforced boundary conditions at the parent grid open boundaries using the MERCATOR global daily reanalysis GLORYS2V4 (Ferry et al., 2012). At the surface, the fluxes of momentum, heat, and freshwater are obtained from hourly outputs of the ERA5 reanalysis (Copernicus Climate Change Service, 2017) using bulk formulas from Large and Yeager (2009). There is no tidal forcing. Vertical mixing is parameterized using a turbulent kinetic energy closure scheme (Blanke & Delecluse, 1993) and bottom friction is quadratic. Both simulations were initialized with temperature and salinity from GLORYS2V4 on 1 January 2005 and run for 2 years for model adjustment. We used daily-mean outputs from the last 10 years of simulation (2007–2016). These configurations resolve the equatorial and near-equatorial current systems and their embedded mesoscale variability. In our simulation, we interpolated the ETOPO2 bathymetry (ETOPO2, 2001) directly into the 1/12° grid. For the NI configuration, we removed grid points with depths shallower than 1,000 m and then linearly interpolated the gaps in the bathymetry prior to running the simulation with the same initial conditions as WI. In practice, this means that this experiment has no islands in the eastern Gulf of Guinea (4°S–6°N, 0°–12°E). However, NI is not fully independent from the islands' influence, since the wind forcing is the same and potential effects of the islands on the wind stress curl would be present in both simulations.

2.3. Data Model Comparison

ADCP observations from the PIRATA/EGEE campaigns (Figure 1a) depict the EUC as a subsurface intensified jet at 6°E, immediately upstream of—and aligned with—São Tomé Island (Figure 1b). The mean observed EUC flows at 0.42 ± 0.2 m s⁻¹, transporting 2.9 Sv within 120 m of water column, with its core at 66 ± 15 m (for the ADCP diagnostics, the standard deviation is obtained from the different available transects at 6°E). Separated by the Equator, westward return flows appear centered at 1.8°N and 1.8°S (Figure 1b). The NEMO 10-year mean (Figure 1c) is consistent with the observed mean EUC, presenting only a slight overestimation in the core velocities, 0.45 ± 0.11 m s⁻¹ at 76 ± 24 m, with transport of 4.1 ± 0.6 Sv, and thickness of 130 m. The westward return flows appear smoothed due to the 10-year average, but present 0.23 ± 0.06 m s⁻¹ and 0.15 ± 0.06 m s⁻¹ (for the Northern and Southern Hemisphere, respectively) close to 90 ± 40 m. (In the model snapshots, core velocity reaches >0.7 m s⁻¹ and the westward return flows reach >0.4 m s⁻¹) Their position (1.5°N and 1.8°S) is also consistent with observations (Figures 1b and 1c). The EUC upstream of São Tomé in both ADCP and the model show values close to the ones reported by Kolodziejczyk et al. (2014), who presented an observed mean velocity of m s⁻¹ and mean transport of 3.7 ± 2.5 Sv at 6°E. From a single cruise (EGEE 5, also used here in our observations ensemble), the authors showed a 100-m-thick EUC, with its core at 70 m. The westward flows in Kolodziejczyk et al. (2014), evaluated at 2.3°E, are further displaced from the Equator, at 2°N and 2.5°S. In our model, the westward jets centered at 1.5°N and 1.8°S at 6°E move poleward, reaching 1.8°N and 2°S at 2.3°E.

To evaluate the modeled EUC vertical structure and salinity, we selected the point closest to the PIRATA moored buoy (0°N, 0°E) in NEMO and interpolated the model vertical levels into the PIRATA 5-m vertical grid. Our NEMO simulation performs similarly to the salinity registered by the PIRATA buoy CTD (Figure 1d), showing median root-mean-squared differences (RMS) values of 0.23 between daily vertical profiles. (We also calculated the correlation with the original PIRATA data, which yielded median values of 0.99, but only ~30% statistically significant correlations.) Overall RMS values (~80%) below 0.3 indicate a good representation of the vertical salinity structure by the model. With comparable mean and standard deviation, 35.6 ± 0.3 for the buoy (Figures 1e) and 35.8 ± 0.5 for the model (Figure 1f), the sharp contrast between surface low salinity and the high salinity associated with the EUC is well captured by the model during the warm season (i.e., no upwelling), when the EUC is strongest. The equatorial upwelling season, which occurs from May–June to August–September (see Picaut, 1983, and earlier references therein), is known to weaken the EUC (e.g., Herbert et al., 2016; Johns et al., 2014) along with its salt transport. The maxima in our model and buoy data are higher and the mean salinity is slightly lower than in Kolodziejczyk et al.'s (2014) observations. This could be due to their sampling periods over two separate months (June and September) outside the period of a strongest EUC (December–May, Figures 1e and 1f) and the peak of the equatorial upwelling season in August (Jouanno, Marin, Du Penhoat, Sheinbaum, & Molines, 2011).

Particularly during the warm season, the model overestimates the vertical extent of the strong subsurface salinity, but the model maximum salinity of 36.8 is consistent with the buoy record of 36.7. In Figure 1d, sudden RMS peaks above 0.3 reveal that the model struggles to fully represent the surface salinity increase due to vertical advection at the beginning of the equatorial upwelling season (e.g., Da-Allada et al., 2017; Jouanno, Marin, Du Penhoat, Sheinbaum, & Molines, 2011). Over time, an increasing salinity trend in the model diverges from the CTD/buoy measurements, leading to an increasing trend in the RMS values. This modeled salinity trend appears to be real, since there were recent reports of a strengthening EUC in 23°W (e.g., Brandt et al., 2021; Stramma & Schmidtko, 2021) that counteracts deoxygenation trends in the tropical Atlantic and might explain the trend depicted from the model. However, for some unknown reason, the PIRATA buoy failed to capture it. A thorough comparison of the EUC characteristics between observations (ADCP and CTD/buoy), NEMO WI, and the literature (Kolodziejczyk et al., 2014) is shown in Table 1.

The main features and dynamics of the eastern Gulf of Guinea are reasonably consistent between observations and model. Assured by the comparisons of this section, we next take advantage of the model's spatial coverage and temporal resolution to track the EUC by its velocity, density limits, and remarkable salinity signal. We ask: what is the influence of the interaction between the EUC and the Gulf of Guinea islands on the region's meso-to-large-scale circulation? We start addressing the islands' influence on the EUC bifurcation and, as we advance on Section 3, our findings motivate new analysis.

Table 1
Summary of the Comparison Between Observations (Shipboard Acoustic Doppler Current Profiler [ADCP] and the Moored PIRATA Buoy Conductivity-Temperature-Depth [CTD]), the Nucleus for European Modeling of the Ocean [NEMO] Reference (WI) Numerical Simulation, and Observations Reported by Kolodziejczyk et al. (2014)

	Observations			Kolodziejczyk
EUC	ADCP (6°E)	CTD (0°)	NEMO	et al. (2014)
Velocity $u\,(\mathrm{m\ s^{-1}})$	0.42 ± 0.2	–	0.45 ± 0.1	0.40
Transport (Sv)	2.9	–	4.1 ± 0.6	3.7 ± 2.5
Thickness (m)	120	–	130	100
Lat. westward flow (°N)	1.8	–	1.5–1.8	2.0
Lat. westward flow (°S)	1.8	–	1.8–2.0	2.5
Mean salinity	–	35.6 ± 0.3	35.8 ± 0.5	35.9
Max. salinity	–	36.7	36.8	36.4
Core depth (m)	60 ± 15	50 ± 14	76 ± 24	70

Note. The CTD core depth is the depth of the maximum salinity.

3. Meso-to-Large-Scale Effects on the EUC Circulation

To study the EUC across the tropical Atlantic basin, we focus on the isopycnal layer bounded on top by the 1,025.3 kg m^{-3} and at the bottom by the 1,026.4 kg m^{-3} isopycnals: the EUC layer. In the Gulf of Guinea between 0° and 6°E, the EUC layer contains the bulk of the EUC's PV anomalies. For each model snapshot, we used the daily model density to delimit the EUC layer and performed a vertical average on each quantity for the grid points within this layer. Then, we time-averaged the individual fields to obtain the mean isopycnal distributions. With our NEMO configuration, the EUC layer in the eastern Gulf of Guinea subset made possible a closer look at the role of the Gulf of Guinea islands in the bifurcation of the EUC, return flows, and associated mesoscale dynamics at ∼9 km resolution.

3.1. The Bifurcation of the EUC

Islands in the Gulf of Guinea interact with the EUC circulation, affecting the distribution of the high salt content brought by the EUC. Figure 2 displays a comparison between the WI and NI NEMO simulations, where the high salinity associated with the mean EUC pathways leaps off the page. For WI, Figure 2a shows the >36 psu salty tongue flowing at ∼0.5 m s^{-1} eastward along the Equator; at 6.4°E, the EUC hits São Tomé Island, bifurcating into northbound and southbound branches. In the shadow zone formed between São Tomé and Príncipe

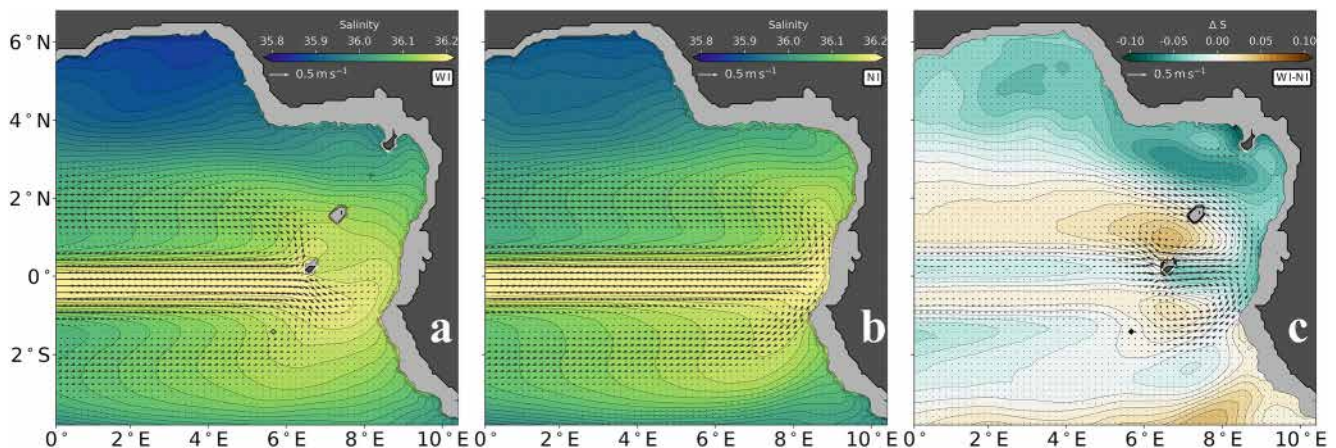**Figure 2.** Mean Nucleus for European Modeling of the Ocean (NEMO) salinity vertically averaged within the Equatorial Undercurrent layer (1,025.3–1,026.4 kg m^{-3}) for (a) the NEMO With Islands (WI) simulation, (b) the NEMO No Islands (NI) simulation, and (c) the difference WI minus NI. The gray shading represents the 100-m isobath. Arrows represent the mean horizontal velocity within the layer.

Islands and the continental shelf, mean velocities are nearly zero, particularly in the Northern Hemisphere. But the salinity is relatively high in the shadow region, indicating salt dispersion by mesoscale activity besides the intermittent eastward advection (notably through the south of São Tomé) by the remnant EUC downstream of the islands in the Southern Hemisphere (Kolodziejczyk et al., 2014). Nevertheless, the obstruction of the EUC flow by the islands partially separates the subsurface high-salinity water from near-surface lower-salinity water—due to high precipitation (e.g., Houndegnonto et al., 2021), the Niger (e.g., Alory et al., 2021) and the Congo (e.g., Awo et al., 2018) river plumes—in the inner Gulf of Guinea, thus weakening the (already high) vertical salinity gradients that influence the surface water in the gulf through vertical advection (Awo et al., 2018). North and south of the Equator, westward return currents leave the domain at 0°E flowing centered at ~2°N and 2.5°S, which is consistent with observations discussed by Kolodziejczyk et al. (2014) at 2.3°E. Subsurface observations in the EUC bifurcation are available mainly through the Argo array (Argo, 2020) and Argo products, for example, Roemmich and Gilson (2009)'s climatology (updated in 2020), in which we were able to observe the bifurcation near São Tomé (not shown). The development and further analysis of such observations are important for a thorough characterization of the EUC termination site.

Without the islands (NI), Figure 2b depicts the EUC flowing past 6°E to terminate off the African continent at the Gabon coast. Curiously, the continental slope drives the EUC to bifurcate in a manner similar to the bifurcation caused by São Tomé in WI. In a model bi-monthly climatology representing the annual cycle of the bifurcation, Kolodziejczyk et al. (2014) showed a bifurcation of the EUC that resembled our NI simulation, with high salinity associated with the EUC often reaching Bioko Island, where the strongest differences appear in Figure 2c. This could be due to the simulation used by Kolodziejczyk et al. (2014), in which the islands do not seem to be well represented on their grid despite the 1/12° horizontal resolution. The differences between the two models are complex to identify and the reasons behind these differences might include the bathymetry interpolation and smoothing, numerical schemes, atmospheric forcing, bulk formula, lateral boundary conditions, and others. In the NI simulation, the meridional spread of the high-salinity tongue is smaller in the region north and south of São Tomé, but the EUC penetrates further east, reaching the northeastern portions of the gulf (Figures 2b and 2c). The westward flows also appear in both hemispheres, at latitudes close to those observed in WI and by Kolodziejczyk et al. (2014)'s observations and model.

Subtracting the salinity and horizontal currents of NI from the WI, Figure 2c shows a slightly weaker and fresher EUC in WI. Most important, it highlights the regions where the presence of islands impacts the general circulation. Due to the earlier bifurcation forced by São Tomé, which prevents the EUC from fully reaching the African continental slope, the strongest differences are observed in the inner portions of the Gulf of Guinea, between Príncipe and Bioko Islands. In WI, the bifurcation at 6°E prevents high-salinity waters from reaching the innermost portions of the gulf, with mean salinity anomalies of −0.18 near Bioko Island and 0.18 near São Tomé related to the penetration of the EUC in NI. North and south of São Tomé, an expected dipolar structure downstream of the island appears with positive anomalies where the EUC bifurcates in WI. Following the path of the westward flows, we note an interesting contrast in the large-scale pattern between hemispheres: the northern westward flow shows a positive salinity anomaly at around 2°N, whereas the southern flow shows a negative anomaly close to 2.5°S.

Zonal currents acting on strong horizontal salinity gradients play an important role on the salt balance in different latitudes of the tropical Atlantic (e.g., Foltz et al., 2004). For the Gulf of Guinea, even though the mean pattern points to a symmetric bifurcation, the distinct anomalies hint at differences in the salt transport back to the western tropical Atlantic. This north-south asymmetry is due mainly to the presence of the islands in the Gulf of Guinea, as we will demonstrate by comparing WI and NI throughout the manuscript. Nevertheless, other potential sources for the asymmetry may also be present in the simulations, such as the wind forcing and the proximity from the continent and its geometry.

The termination of the EUC in the WI simulation in Figure 2a is analogous to the Pacific EUC termination at the Galápagos Archipelago described from model analysis (e.g., Karnauskas et al., 2007), ADCP data (e.g., Karnauskas et al., 2010), and glider observations (e.g., Jakoboski et al., 2020). In the Pacific, however, the bifurcation caused by the islands continues flowing east, with most of the flow joining the continental slope (cf. Karnauskas et al., 2007; Karnauskas et al., 2010; Montes et al., 2010) toward both hemispheres. Here, this is partially true for the Southern Hemisphere, where a remnant of the EUC flows southeastward before veering west. However, for the Northern Hemisphere, the presence of islands forces the flow westward, with no organized mean flow east of 6.5°E as seen in NI. A major difference between the Atlantic and Pacific cases resides in the

return flows. Although they were also observed in the Pacific (e.g., Johnson et al., 2002), only a lesser portion of the Pacific EUC veers west to support their formation (Karnauskas et al., 2007, 2010; Montes et al., 2010). In the Atlantic, these mean westward flows are a consequence of the successive westward-propagating mesoscale eddies generated during the bifurcation of the EUC in the inner portions of the Gulf of Guinea (Assene et al., 2020).

We showed how the islands (particularly São Tomé) block the EUC, preventing salty waters to reach the inner-most portions of the gulf. At a first glance, no remarkable change in the returning westward flows were observed, since the bifurcation also occur in NI, which leads us to question: does the presence of islands only impact the circulation locally, or are there consequences to the net fluxes across the Atlantic? To answer this question, we further explore the role played by islands in the EUC bifurcation and westward returning flows. To better track the origin of the bifurcation and eddies, as well as the changes undergone by the EUC during eddy formation, we perform a PV analysis in the EUC layer, focusing on the eastern portions of the Gulf of Guinea.

3.2. Gulf of Guinea Islands and Mesoscale Dynamics of the EUC

PV is a key quantity in the interpretation of ocean dynamics due to its strong link with circulation, conservation along isopycnals, and inversion properties (Bretherton & Haidvogel, 1976; Hoskins et al., 1985; Morel et al., 2019). According to Rhines (1986), geostrophic turbulence develops regions of homogenized PV and specific circulation patterns. In quasigeostrophic models, this circulation is fundamentally associated with the PV anomaly, calculated with respect to a background PV at rest. Since this background PV—simply equal to the Coriolis parameter for the quasigeostrophic model—varies spatially with latitude, meridional advection can lead to local PV anomalies and alter the circulation. Indeed, there is a quantitative link between the integrated PV anomaly and the barotropic circulation or transport (e.g., Morel et al., 2019). While PV is conserved for adiabatic evolution, friction and diapycnal mixing can in turn modify the PV and create anomalies, generating circulation patterns. In the present study, we analyze the differences between the WI and NI circulations through their PV structures.

In the study of equatorial zonal jets, the well-known PV structure is characterized by a meridional inversion of homogeneous PV and strong gradients at each side of the jets (cf., Fofonoff & Montgomery, 1955; Pedlosky, 1987; Pedlosky & Spall, 2015). Along the Equator, low-PV waters and weak zonal gradients characterize the core of the flow (e.g., Delpech et al., 2020; Ménesguen et al., 2009). Usually, PV within the pycnocline is dominated by the strong background signal of the stratification at rest, making it difficult to distinguish horizontal anomalies related to the "dynamically-active" PV (e.g., eddies). To overcome this limitation, Morel et al. (2019) proposed an alternative calculation for PV, in which a rescaling allows the interpretation of the evolution of PV anomalies along isopycnic surfaces, as proposed by Hoskins et al. (1985). The rescaled PV has the same conservation properties as the Ertel PV—boiling down to the quasigeostrophic PV when geostrophic and hydrostatic approximations are made—but compensates for the signature of the pycnocline that would otherwise dominate the Ertel PV. Previously used by Delpech et al. (2020) and Assene et al. (2020) in the study of equatorial jets, Morel et al.'s (2019) rescaled PV

$$Q = (\zeta + \mathbf{f}) \cdot \nabla G_\rho \tag{1}$$

is obtained using a specific function G_ρ based on potential density and chosen so that for all density levels the PV at rest associated with a reference density profile is equal to the vertical component of the planetary vorticity. In Equation 1, ζ and $\mathbf{f}$ are the 3D relative vorticity and Earth rotation vector, respectively. In considering primitive equations, we neglect the vertical velocity terms in ζ and use only the vertical component of $\mathbf{f}$, that is, the Coriolis parameter $f = 2\Omega\sin(\varphi)$—where φ is the latitude and $\Omega = 7.29 \times 10^{-5}$ s^{-1}—and $\zeta = (-\partial_z v, \partial_z u, \partial_x v - \partial_y u)$. G_ρ is the rescaling function responsible for masking the background stratification effect on PV (cf. Morel et al., 2019). It is based on a reference density profile representative of the PV at rest and has units of meters. To obtain this reference density ρ_r, we tested several density profiles aiming to reduce the effect of stratification on PV, and chose a 10-year mean profile averaged in a 0.5°box around (1.5°N, 8.5°E), so $\rho_r = \overline{<\rho>}$. The area is close to the choice for reference profile by Assene et al. (2020) using a similar NEMO configuration. Unlike Assene et al. (2020), we opt here for a spatio-temporal-averaged profile which nevertheless presents the desired characteristics for rescaling the PV, such as low surface densities and stratification typical of the pycnocline at rest (Assene et al., 2020; Morel et al., 2019).

The mean horizontal distribution and standard deviation of the PV in the EUC layer is displayed in Figure 3. Away from the continent (i.e., from ~0 to 5°E), both WI and NI simulations show the inversion in PV typical
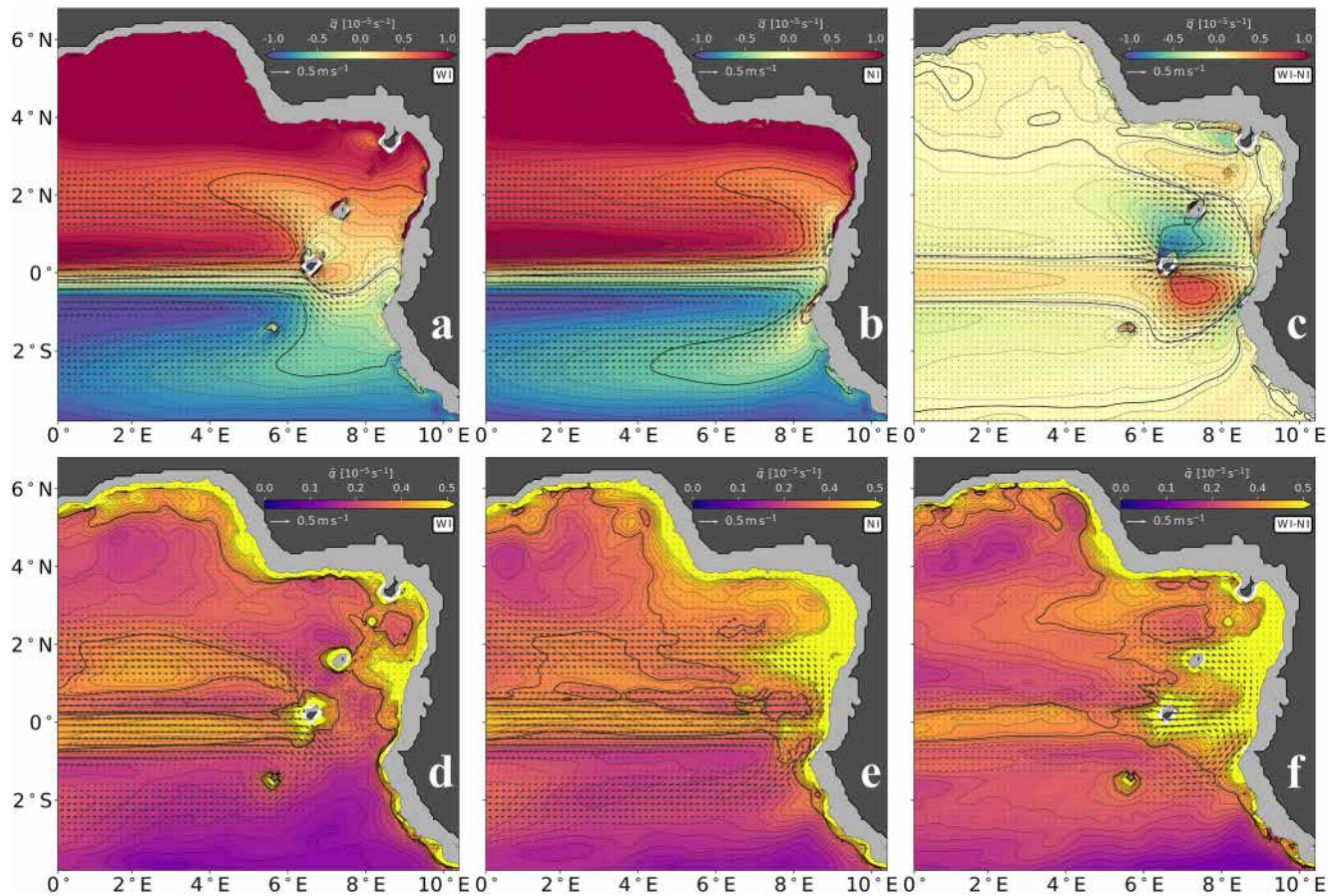
Figure 3. Potential vorticity (PV) in Nucleus for European Modeling of the Ocean experiments. (a–c) Mean PV vertically averaged within the Equatorial Undercurrent (EUC) layer (1,025.3–1,026.4 kg m^{-3}) for the With Islands (WI) simulation (a), the No Islands (NI) simulation (b), and the difference between WI and NI (c). Thick black lines represent $|Q| = 0.6 \times 10^{-5}$ s^{-1}. The gray shading represents the 100-m isobath. Arrows represent the mean horizontal velocity within the layer. (d–f) PV standard deviation within the EUC layer for WI (d), NI (e), and the difference between WI and NI (f). Thick black lines represent the standard deviation of 0.35×10^{-5} s^{-1}.

of equatorial jets (Figures 3a and 3b): from the Southern Hemisphere ($\sim$1°S) to the north, PV is negative and increases northward, crossing the low PV band ($Q \approx 0$) around the Equator to show strong positive values at $\sim$1°N. Approaching 6°E, however, Figure 3a displays the bifurcation of the low-PV waters ($|Q| < 0.6 \times 10^{-5}$ s^{-1}) associated with the core of the EUC (and also with the maximum salinity region in Figure 2a) and their spread across the shadow area downstream of the islands. The presence of São Tomé Island also acts to redirect the low PV of the EUC southeastward, forming a meander before reaching the African coast. In the lee of São Tomé, weak mean velocities and high variability point to transient mesoscale features playing a major role in spreading the EUC low PV eastward (also shown in the PV animations available in this study's in Supporting Information S1). Moreover, positive anomalies east of the island (0°N, $\sim$7°E) and patches of weaker negative anomalies north and northeast of the island ($\sim$1°N, $\sim$7°E) show local PV anomalies due to interaction between the EUC and São Tomé. Thus the PV variability account for both adiabatic (change of path of the current imposed by kinematic boundary conditions) and diabatic (friction and mixing close to the islands) effects. As described in Figure 2b, the bifurcation in NI occurs at the continental slope; the zonal spread is smaller, but the low-PV/highest-salinity waters reach the innermost portions of the gulf (Figure 3b). As seen in the difference between WI and NI (Figure 3c), the mean effect of the islands on the PV is the presence of PV dipoles in the vicinity of the islands (e.g., Pedlosky & Spall, 2015). The biggest structure is located downstream of São Tomé, but similar features can be seen near Príncipe, Bioko or even Annobón (2°S, $\sim$6°E).

Away from the Gulf of Guinea, in both experiments, two PV tongues extending westward from their respective bifurcation sites indicate the main fate of the EUC waters (Figures 3a and 3b). As previously reported, the PV tongues are a reflex of the current termination in a bifurcation (Kolodziejczyk et al., 2014) and the formation

of westward-propagating mesoscale anticyclonic eddies (Assene et al., 2020). The remarkable observation here is the westward extension of the strong low-PV signal, which shows an asymmetry between the WI and NI experiments. In Figure 3a, the Northern Hemisphere $|Q| < 0.6 \times 10^{-5}$ s^{-1} tongue reaches 4°E, while its Southern Hemisphere counterpart stops at ~6°E. The opposite is observed in the NI case (Figure 3b), which is consistent with differences between the simulations in respect to the saltier waters advected westward by the eddies noted in Figure 2c.

The temporal variability of PV (Figures 3d–3f) shows a zonal band of relatively high variations in PV along the Equator. Part of this variability is adiabatic and does not necessarily indicate PV transformation. Instead, these variations may occur due to seasonal and interannual latitudinal migration of the main axis of the EUC (Brandt et al., 2014; Jouanno et al., 2013). Studying the seasonality of the surface cooling in the Gulf of Guinea with a numerical model, Jouanno et al. (2013) noted this EUC core meridional migration. Later, using mooring and shipboard velocity measurements and an EOF analysis, Brandt et al. (2014) identified latitudinal excursions of the EUC core, represented by both southward and northward anomalous displacements. The authors linked this process to an interannual variability, consistent with the timescale of the variability of basin-mode oscillations due to the eastward propagation of equatorial Kelvin waves and the rebound of westward long equatorial Rossby waves (cf. Cane and Moore 1981; see also Brandt et al., 2011). However, intermittent processes also play a role, with friction and diapycnal mixing being able to drastically modify the PV distribution within an oceanic current (e.g., Morel & McWilliams, 2001). In particular, the strongest PV variations in Figures 3d–3f occur near topography, with clear hotspots of variability around the islands (Figure 3d). These locations might indicate sites of diabatic PV transformation. There, friction likely plays a major role in transforming PV (e.g., Benthuysen & Thomas, 2012; D'Asaro, 1988; Morel & McWilliams, 2001), but we acknowledge that staircase bottom and lateral walls (as well as wind stress, to a lesser extent at the EUC depth, ~80 m) in the model may add to this effect. In Figure 3d, an east-west band of high PV variation between 1 and 2°N points to São Tomé as the source of this variability, although its presence also in NI (Figure 3e) prevents us from pinpointing its association with the islands.

The PV maps in Figures 3d and 3e hint at flow-topography interactions as a major process responsible for creating PV anomalies in both simulations, whether with the islands in WI or the African continent in WI and NI. In terms of the mean circulation pattern (Figure 3), friction with land generates anticyclonic PV anomalies. Indeed, Assene et al. (2020) showed that anticyclonic eddies generated from PV anomalies in the Gulf of Guinea propagate west through the tropical Atlantic in eddy corridors between 4°S and 4°N. However, local friction effects at shorter time scales are far more complex—generating both anticyclonic and cyclonic anomalies—and should not be estimated solely from Figure 3, which leads us to question: do EUC-islands interactions (particularly São Tomé) play a role in the formation and distribution of such eddies? Moreover, can these interactions shape the EUC return flows and transform its PV?

3.3. Extra-Equatorial Westward-Propagating Eddies

In the Gulf of Guinea, the EUC arriving at the easternmost portions of the gulf triggers the formation of mesoscale anticyclones that propagate westward, toward the direction of the incoming flow (e.g., Assene et al., 2020). A sequence of PV snapshots in Figure 4 illustrates the extra-equatorial eddy corridors during a period of strong eddy activity. In both simulations, anticyclonic eddies are formed in both hemispheres and propagate westward at ~0.11 m s^{-1} (10 km day^{-1}). However, comparing the eddies in WI and NI, differences in their size and strength can be depicted. On 27 December 2007, Figure 4a captures an anticyclone forming at 5°E northwest of the Gulf of Guinea islands; at ~1°E, a pinched-off eddy propagates westward, with a trail of low PV suggesting deformation due to lateral shear between the eddy and the EUC. In the Southern Hemisphere, a weaker low-PV signal leaves the region at ~2°S. The following snapshots, after 30 and 60 days (Figures 4b and 4c, respectively), show the evolution of the flow, with strong ~100-km-radius eddies traveling in the north corridor, and smaller, faint eddies occurring in the Southern Hemisphere. In the NI simulation, the EUC still bifurcates, but its bifurcation occurs at the African continental slope rather than at ~6°E. Figure 4d shows, in both hemispheres at ~8°E, the nearly symmetric formation of eddies which propagate westward at velocities similar to those in WI. However, in NI the larger and stronger eddies appear in the Southern Hemisphere (Figures 4e and 4f). This eddy-formation pattern is recurrent throughout the model timeseries, as discussed below.

To better compare the evolution of the flow in WI and NI, we analyze the meridional structure of the PV together with the energy associated with eddies. We distinguish the low-PV regions (regardless of the PV sign) and their
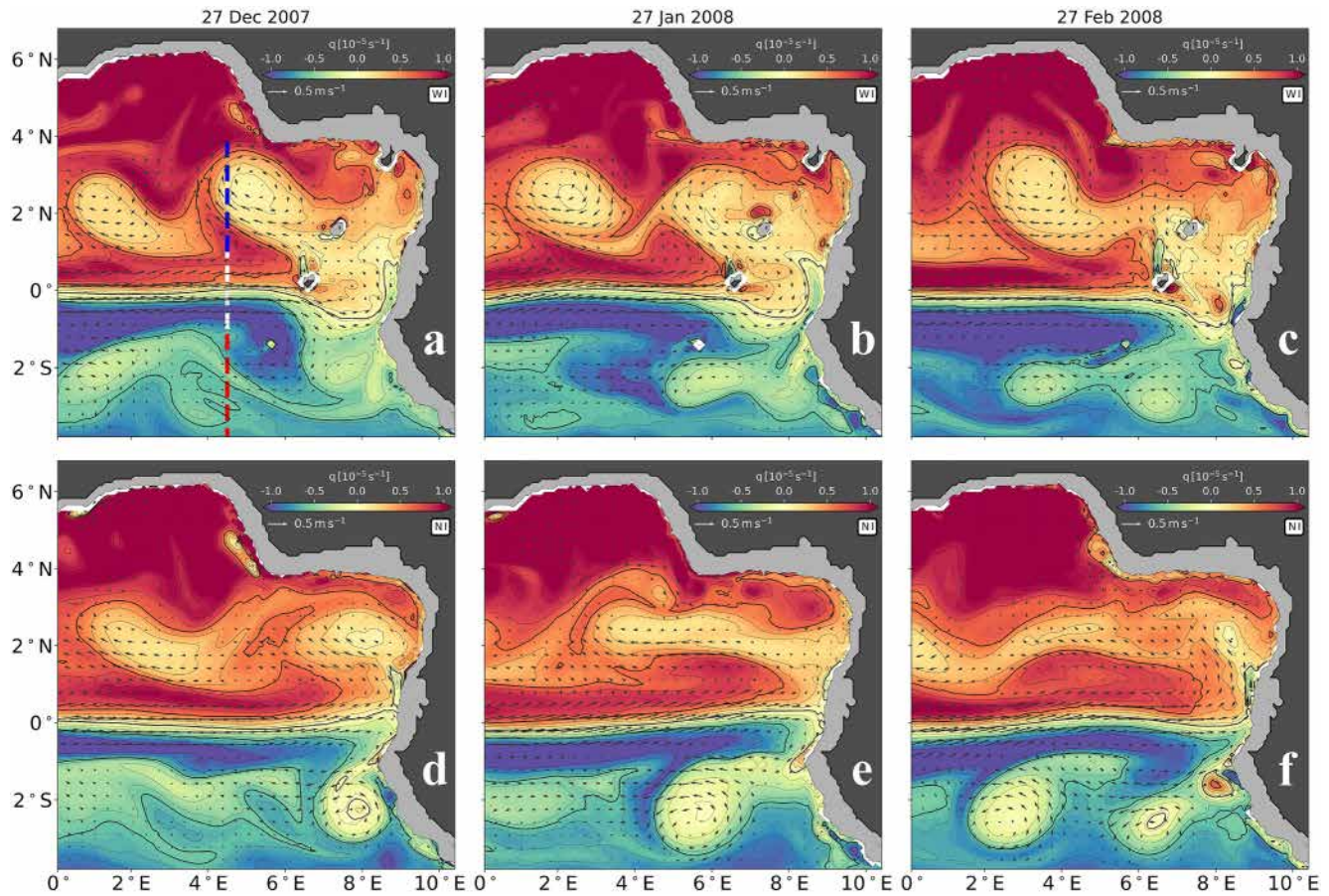
Figure 4. Snapshots of Nucleus for European Modeling of the Ocean (NEMO) potential vorticity (PV) vertically averaged within the Equatorial Undercurrent layer (1,025.3–1,026.4 kg m^{-3}) for the (a–c) NEMO With Islands simulation and (d–f) NEMO No Islands simulation. (See animations in the Supporting Information S1 of this paper.) Thick black lines represent $|Q| = 0.6 \times 10^{-5}$ s^{-1}. The gray shading represents the 100-m isobath. Arrows represent a subset of the horizontal velocity vertically averaged within the layer. The meridional section in (a) is used to quantify the PV and salt fluxes in the Equator (white) and North (blue) and South (red) Hemispheres.

associated eddy activity by calculating the longitudinally averaged, meridional profiles of the potential enstrophy (Q^2) and eddy kinetic energy (EKE = $\tilde{u}^2 + \tilde{v}^2$, where the tilde represents the anomaly from a low-pass filter of 60 days) of the EUC. Figure 5 shows the median values of EKE (Figure 5a) and Q^2 (Figure 5b) meridional profiles for WI superimposed on NI, in zonally averaged bands spanning 3° from 0° to 9°E. Between 1°S and 1°N, both simulations show nearly coincident high EKE and low enstrophy (and consequently low PV) from 0° to 6°E, with two local maxima around a local minimum at 0°. In the easternmost profile, this pattern is less evident but still present in NI's Q^2 (Figure 5b), while in EKE and in WI's Q^2 the pattern collapses due to the bifurcation. The low PV extends to about 2° meridionally from the Equator, developing local PV anomalies with respect to the higher PV background at ~2°N and 2°S. The roll up of these low-PV anomalies into eddies occurs in both simulations, but at different longitudes. Nevertheless, they propagate westward through the same eddy corridors, centered at ~2° on both sides of the Equator. This allows a qualitative comparison between the EKE maxima associated with a Q^2 minima in both hemispheres. The median values of WI in Figure 5 show higher values of EKE and smaller values of Q^2 in the return flow north of the Equator compared to NI, while the opposite (that is, NI's EKE [Q^2] greater [smaller] than WI) is observed south of the Equator.

Considering that the incoming EUC has virtually the same EKE and Q^2 in both experiments, the median difference implies that in WI, stronger eddies carrying more low-PV are generated in the Northern Hemisphere than in the Southern Hemisphere and that the opposite is true in NI. An overlap within 60% of the EKE and Q^2 distributions (0.2 and 0.8 quantiles) between the two simulations is consistent with the recurrent presence of low-PV eddies in both hemispheres for WI and NI; their presence in both simulations further points to stronger eddies responsible for the north-south asymmetry around 2°N and 2°S (Figures 5a and 5b). This asymmetry could be
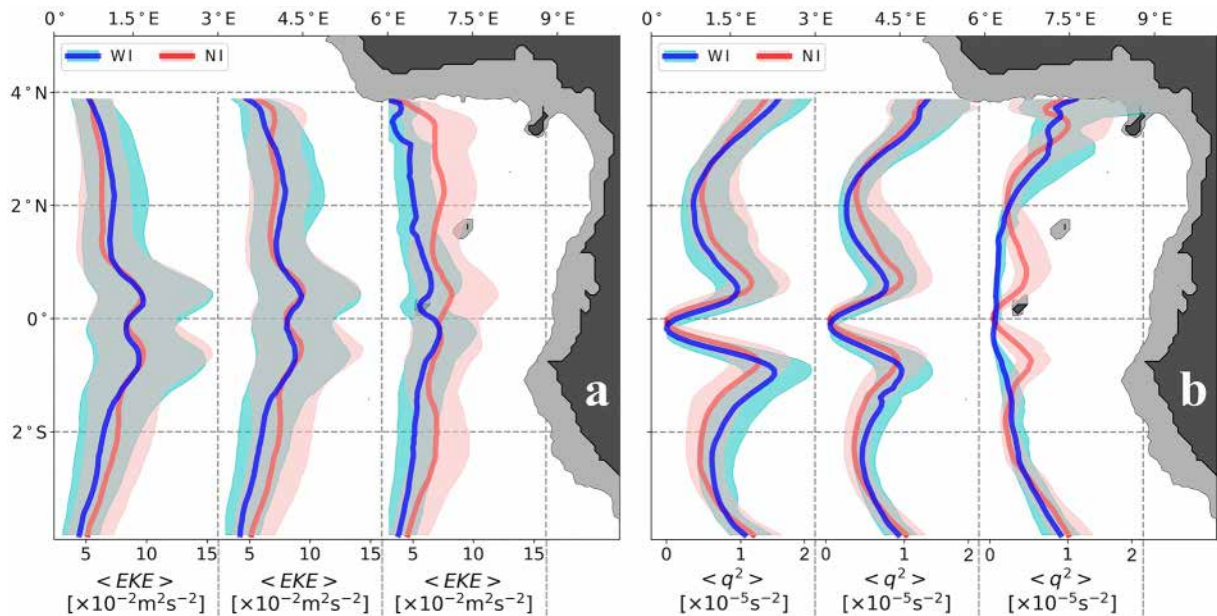
Figure 5. Zonally averaged (a) eddy kinetic energy and (b) potential enstrophy profiles within the Equatorial Undercurrent layer (1,025.3–1,026.4 kg m^{-3}) between 0 and 3°E, 3–6°E, and 6–9°E. Lines represent the median values for the Nucleus for European Modeling of the Ocean (NEMO) With Islands (blue) and the NEMO No Islands (red) simulations. The light blue and light red bands around the lines represent the interval between the 0.2 and 0.8 quantiles.

due to the suppression of symmetric instability modes in the presence of islands, one of the distinct unstable modes that lead to eddy formation in the EUC (e.g., McCreary & Yu, 1992).

Below, we investigate how the interaction between the Gulf of Guinea islands and the EUC dynamics is responsible for the apparent difference in eddy generation between hemispheres depicted in Figures 3–5. For the meridionally-alternating flows associated with the EUC, we calculated the PV and salinity fluxes across a meridional section at 4.5°E (see the meridional transects in Figure 4a). The transects span 1°S–1°N, 1–4°S, and 1–4°N for the Equator, southern, and northern paths, respectively. For the flux Φ of a quantity A advected across these meridional sections,

$$\Phi = \iint_S (uA)\, dy\, dz \tag{2}$$

u is the zonal velocity crossing the section within a low-PV region, and dy and dz are the "steps" in latitude and depth range of the meridional section. In this analysis, y varies for the Equator, south, and north sections at 4.5°E as described above. The thickness z is the distance between the isopycnals of the EUC layer. We restricted the analysis to the EUC core (1,025.3 kg m^{-3} < ρ < 1,026.4 kg m^{-3}) and the PV anomalies that originated from this waters; in practice, outside the region of low PV (|Q| < 0.6 × 10^{-5} s^{-1}), we set the velocity u = 0. With u representing only the low-PV flow and zero elsewhere, we use Equation 2 with $A \equiv \rho S_a$ (S_a: absolute salinity) and $A \equiv Q$ to obtain the salt and PV fluxes, respectively.

The EUC advects salt into the Gulf of Guinea by carrying SMW and SACW from the western tropical Atlantic (e.g., Stramma & Schott, 1999). Within its core, the highest values of salinity are associated with low values of PV, which are also related to the PV anomalies that form the westward-traveling mesoscale eddies (Figure 4). At these depths, the connection between the western and eastern sides of the tropical Atlantic is thus dominated by—but not restricted to—the eastward and westward fluxes within the low-PV band of the EUC. For the incoming EUC, Figure 6a shows similar incoming fluxes for both WI and NI, with the EUC advecting on average 93 ± 39 × 10^6 kg s^{-1} into the domain between 1°S and 1°N, with peaks above 150 × 10^6 kg s^{-1} (maximum 212 × 10^6 kg s^{-1}). These peaks show an ∼120-day variability, consistent with the period of equatorial Kelvin waves at this depth (e.g., Bachèlery et al., 2016; Illig & Bachèlery, 2019; Polo et al., 2008). The effect of Kelvin waves can be crucial to deepen the EUC core by modifying the thermocline slope (Hormann & Brandt, 2009), thus affecting the depth at which the EUC hits the island. As a consequence, the flow meets a larger bathymetric

Figure 6. Low-pass filtered (7 days) daily salt fluxes at 4.5°E for the (a) eastward-flowing Equatorial Undercurrent between 1°S and 1°N, (b) Northern Hemisphere westward return flow between 1 and 4°N, and (c) Southern Hemisphere westward return flow between 1 and 4°S. Orange lines represent the With Islands simulation, and cyan lines represent the No Islands simulation. The legend boxes show the integrated transport for the 10-year model series in Eg, (exagram = 10^{15} kg), with yearly percentages of westward transport (b, c) relating the transport in each hemisphere to the total eastward transport at the Equator for the period.

signature of the island, and flow-island interactions tend to strengthen (recall the model island's bathymetry from Figure 1). Figures 6b and 6c show the westward salt flux between 1–4°N and 1–4°S, respectively. In both cases, we observe strong variability, with peaks in the salt flux interposed with periods of zero transport, consistent with the intermittent passage of low-PV vortical structures. In the Northern Hemisphere (Figure 6b), transport peaks due to eddies are stronger in the WI simulation, whereas in the Southern Hemisphere (Figure 6c), the peaks due to mesoscale eddies appear mainly in the NI simulation. Time-integrating Equation 2 for the 10-year time series yield a total salt input of ~30 Eg (1 Eg ≡ 1 exagram = 10^{15} kg). *That is equivalent to more than 50 million RMS Titanics fully loaded with salt traveling from west to east and back every year!* (Or about 6 million times the capacity of the largest modern container ships.) After the incoming EUC breaks up into westward-propagating anticyclonic eddies, the WI salt flux integrated on the north corridor accounts for $47 \pm 5\%$ of the influx, and the south path transports only $23 \pm 4\%$ (orange lines in Figures 6b and 6c). In NI, the asymmetry is virtually nonexistent, with $39 \pm 5\%$ of the incoming flow returning west through the north corridor and $32 \pm 2\%$ through the south corridor (cyan lines in Figures 6b and 6c).

The difference between the north and south corridors goes beyond the percentages of return flux expressed above. In Figures 6b and 6c, peaks related to eddies in NI present comparable formation periods and strength for both hemispheres. For WI, however, differences in the number and strength of the eddies between hemispheres appear: while weak and rare in the Southern Hemisphere, eddies in the north corridor are numerous and grow

much stronger. The distribution of the peaks in Figures 6b and 6c shows that eddies also present seasonal and interannual variability related to the EUC's variability depicted in Figure 6a.

Every year, eddies are generated preferentially from December to June (Figure 6b). This aligns with the notion that a strong EUC is essential to the formation of the anticyclonic eddies, seeing that, from June to November, the equatorial upwelling season weakens the EUC (e.g., Herbert et al., 2016; Johns et al., 2014; Jouanno et al., 2013) and eddy occurrence is smaller (Figures 6b and 6c). Moreover, the strongest eddies in the model occur in WI for the Northern Hemisphere, where a strong EUC interacts with São Tomé. Particularly in 2008, 2009, and (less evident in) 2013, the strongest events in WI ($>100 \times 10^6$ kg s^{-1}; Figure 6b) stand out from the series. This is probably due to the northward shift of the EUC at 6°E during these periods, which is consistent with strong flow-island interactions (note in our model's PV animation in Supporting Information S1 that São Tomé Island is located somewhat on the northern side of the equator). Such meridional displacements of the EUC are due to the current's interannual variability (e.g., Brandt et al., 2014). The meridional shift in our simulation is opposite to that which Brandt et al. (2011) reported at 23°W (southward). At 6°E, where São Tomé Island is, the shift is indeed opposite to Brandt et al.'s.

Taking N_c and S_c as the salt transported westward through the north and south corridors (Figures 6b and 6c, respectively), we can quantify the EUC split between hemispheres:

$$\sigma = \frac{N_c}{N_c + S_c} . \tag{3}$$

In the WI simulation, $\sigma_{\mathrm{WI}} \approx 2/3$ indicates that the asymmetry imposed by the islands is quantitatively significant. In the absence of islands, $\sigma_{\mathrm{NI}} \approx 1/2$ points to a symmetric bifurcation at the African continental slope, with westward flows mirrored by the Equator. Another simple yet useful relation,

$$\lambda = \frac{N_c + S_c}{I_e} \tag{4}$$

accounts for the loss of the incoming EUC (I_e) waters within the innermost portions of the Gulf of Guinea. The ratio $\lambda_{WI} \approx \lambda_{NI} \approx 0.7$ indicates a 30% loss of salt content in both simulations. Possible reasons accounting for this imbalance include fluxes of EUC waters to higher latitudes and diapycnal mixing, which leads to exchanges between the upper and lower layers. As far as PV fluxes are concerned, the advection of PV anomalies by westward-propagating eddies (not shown) follows the same pattern as salinity (with opposite sign on the Southern Hemisphere), which is not surprising, since PV and salinity are somewhat homogeneous within the eddies.

The variability of the EUC and its interaction with the islands of the Gulf of Guinea introduce an asymmetry to the transport of tracers via eddy corridors in the Northern and Southern Hemispheres. This occurs mainly due to the formation of stronger and more numerous eddies in the Northern Hemisphere in WI. Moreover, salinity and PV, as they are transported by those eddies, are also modified within the Gulf of Guinea. While changes in the salinity are only due to mixing, PV is also modified by friction. This notion is now used to separate the influence of both effects on the PV diabatic evolution. Finally, both processes being strengthened locally around the islands, we are encouraged to focus on the encounter between the EUC and São Tomé, where regional processes comes into play in the transformation of the EUC waters during the current's bifurcation and eddy generation.

4. Changes in the EUC Around the Gulf of Guinea Islands

During bifurcation, the EUC naturally generates eddies with or without islands due to different unstable modes (e.g., McCreary & Yu, 1992). Flow-topography interactions can change this instability, being responsible for the generation of mesoscale features (e.g., Jouanno & Capet, 2020) that escalates to alter larger-scale dynamics through geostrophic turbulence and the inverse energy cascade (cf. Charney, 1971; Hoskins et al., 1985). An eddy carrying a PV anomaly from east to west in an ocean basin translates into an input of eddy kinetic energy proportional to the eddies' enstrophy (e.g., Li et al., 2018). In the Gulf of Guinea, the propagation of these low-PV eddies introduces PV anomalies that affect the dynamics throughout their westward paths in the tropical Atlantic. Therefore, in this section, we use PV diagnostics to infer how diapycnal mixing or other mechanisms (such as friction and isopycnal mixing) can modify the EUC waters, and we propose a rough estimation of their effects. We first evaluate the mean PV of parcels entering the area within the EUC and then leaving in the core of eddies,

forming the north and south return flows. Modification of this quantity is necessarily associated with diabatic effects. To evaluate the diapycnal fluxes in and out of this layer causing the PV modification, we note that the volume of the EUC layer varies only because of diapycnal mixing, since isopycnal mixing does not change the EUC layer volume bounded by two isopycnal levels. These fluxes can be used to infer the effect of diapycnal mixing on PV, with the remaining PV changes being accounted for other processes (friction and mixing along isopycnal surfaces). Finally, since the dynamics and the vorticity of eddies reflect the PV anomaly (with respect to the local planetary vorticity for the rescaled PV), meridional displacements have to be considered, too.

4.1. PV Anomalies in the EUC

In our modeled EUC in the eastern Gulf of Guinea, local PV anomalies can derive from meridional advection of PV, with low-PV EUC waters moving into a high-PV background due to the bifurcation of the EUC, leading to positive and negative anomalies in the Southern and Northern Hemispheres, respectively (e.g., Assene et al., 2020, see also Figure 4). Due to conservation of PV, these opposite PV anomalies in different hemispheres will develop an anticyclonic circulation proportional to the strength of the meridional displacement (Assene et al., 2020; Morel et al., 2019). Local effects of friction and diapycnal and/or isopycnal mixing also change the PV distribution (e.g., Morel & McWilliams, 2001). In the present study, the estimation of PV and salinity fluxes gives us some indications about the processes involved in the generation of eddies and modification of the circulation in the vicinity of the islands. Indeed, in an isopycnal layer, mixing and friction are both important to generate PV anomalies that develop into eddies.

The PV evolution equation for each Lagrangian particle is a combination of advection, diapycnal mixing, and friction terms (Müller, 2006, see also, e.g., Gula et al., 2019; Thomas, 2005). Cast in the Eulerian form,

$$\partial_t Q = -\operatorname{div}\left(\underbrace{\mathbf{u}\, Q}_{\text{advection}} + \underbrace{\nabla G_\rho \times \mathbf{F}}_{\text{friction}} - \underbrace{(\boldsymbol{\zeta} + \mathbf{f})\frac{dG_\rho}{dt}}_{\text{diapycnal mixing}} \right), \tag{5}$$

the PV evolution is the sum of the individual terms in the right-hand side of Equation 5, where **u** is the advection velocity, F represents friction and other nonconservative forces (e.g., Gula et al., 2019; Thomas, 2005), and dG_ρ/dt accounts for diapycnal mixing effects. To obtain rigorous quantitative budgets of Equation 5, we need daily diapycnal mixing and friction terms for each particle. Although this is not possible in the present experiments, qualitative estimates of PV transformation within the Gulf of Guinea can be drawn from the following approach and assumptions:

- the mean flow (over the 10 years of simulation) is constrained within Northern and Southern Hemisphere streamtubes of volume V, connecting the northern and southern exit sections to entrance sections within the EUC. The streamtube is bounded vertically by the EUC layer and laterally by mean circulation streamlines;
- for each streamtube, we assume the initial/entrance PV can be estimated using the mean PV over their respective EUC section (even though the streamtubes may represent only a fraction of the EUC section);
- volume variations within each streamtube are predominantly due to diapycnal fluxes, while lateral fluxes are negligible (as shown in Figures 2 and 3, mean velocities are weak at the edge of the streamtube, with associated fluxes representing less than 5% of the EUC incoming fluxes);
- the incoming EUC transport V_{EUC} to each hemisphere follows the same ratio as the split between hemispheres at the exit (i.e., Equation 3 applied to the volume flux instead of salinity). This is a rough approximation, but sufficient to get an order of magnitude for the effect of diapycnal mixing on the PV budget.

The approach and assumptions above (detailed in the Supplementary Information S1) allow us to use mean volume flux to estimate the changes in the mean PV values of the EUC. The mean values are defined by dividing the PV flux by the volume flux to obtain average values entering and leaving the domain through the streamtubes. For the flow that returns westward, the final mean PV advected at the exit section is thus the initial mean PV plus anomalies imposed by diapycnal mixing and other processes, which include friction and isopycnal mixing (and also possible effects due to wave-flow interaction and errors associated with numerical schemes and with the diapycnal mixing estimation). At the exit section,

$$Q_f = Q_{\text{EUC}} + \delta Q_{\text{mix}} + \delta Q_{\text{other}} \tag{6}$$
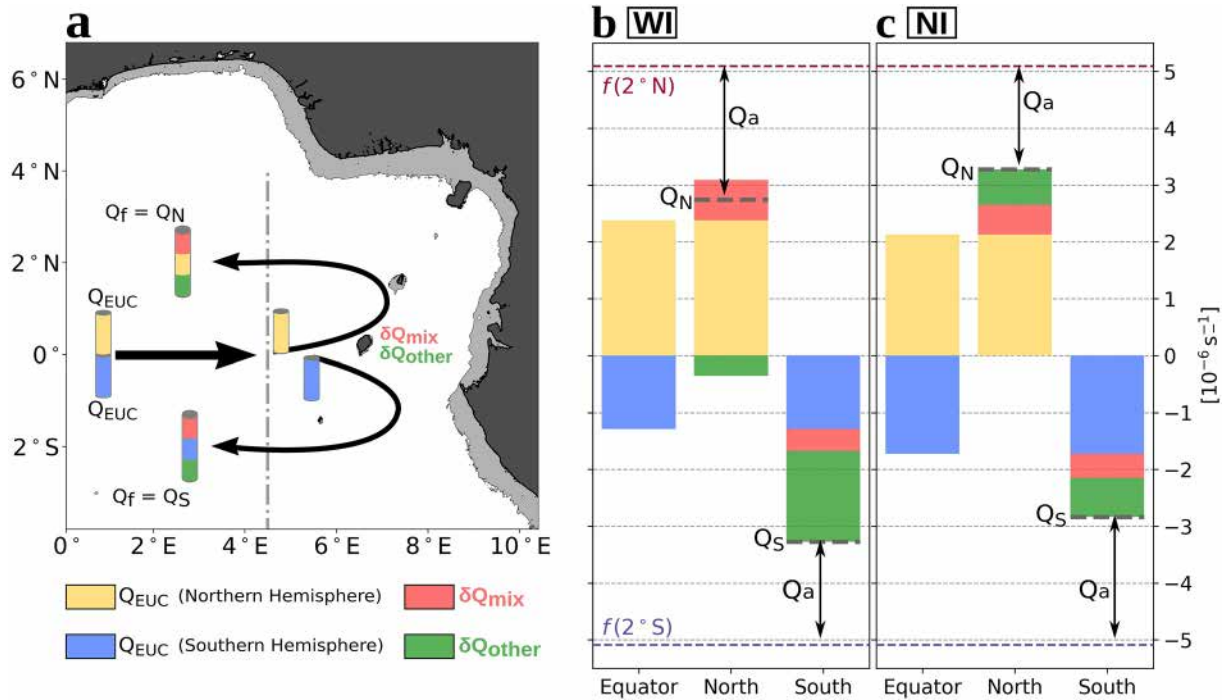
Figure 7. Changes in the Equatorial Undercurrent (EUC) potential vorticity (PV) due to diapycnal mixing and other processes in the Gulf of Guinea. (a) Schematic representation of the problem addressed, where the initial Q_{EUC} at each hemisphere may be transformed by processes within the Gulf of Guinea and return as westward flows. The final Q_f at each hemisphere is the result of this hemisphere's bulk Q_{EUC} modified by different δQ_{mix} and δQ_{other}. (b) PV transformation in the WI experiment. (c) PV transformation in the NI experiment. Gray dashed lines show Q_f at each hemisphere (Q_N or Q_S; the sum of the bars). Q_{EUC}: initial bulk PV of the EUC at 4.5°E for each hemisphere; Q_N: PV across the northern transect at 4.5°E; Q_S: PV across the southern transect at 4.5°E; δQ_{mix}: PV transformation due to mixing; δQ_{other}: PV transformation due to friction and isopycnal mixing; Q_a: strength of the PV anomaly with respect to the background planetary vorticity.

where Q_{EUC} is the mean EUC PV at the Equator and Q_f represents the mean outgoing PV, with $Q_f = Q_N$ and Q_S for the northern and southern streamtubes, respectively.

We consider eastward-flowing water columns with mean Q_{EUC} bifurcating in the east Gulf of Guinea (Figure 7a). In our assumptions, the incoming Q_{EUC} has different values for each hemisphere/streamtube; at these locations, δQ_{mix} and δQ_{other} modify the incoming PV independently. The PV transformation due to diapycnal mixing is a function of the initial PV and the volume change (see Haynes & McIntyre, 1987, and Section S3 in the Supporting Information S1),

$$\delta Q_{mix} = -Q_{EUC}\frac{\delta V}{V_f} \tag{7}$$

where V_f is the final volume of the layer with a $\delta V = V_f - V_{EUC}$ increment associated with diapycnal mixing. In Equation 7, the transformation of the mean PV of the water column due to diapycnal mixing is proportional to its variation in volume. In our simulations, the total variation of volume for both hemispheres $\delta V \approx -0.25$ Sv is negative, showing that there is a net flux of EUC water into the lower layer because of mixing.

The results for the PV transformation in the EUC are summarized in Figure 7, where we illustrate the processes which modify the EUC PV along its path (Figure 7a). For particles flowing into the Gulf of Guinea, diapycnal mixing as well as other processes modify the initial Q_{EUC}. During bifurcation, the EUC branches charge across the planetary vorticity gradient, developing local PV anomalies ($Q_a = Q_f - f$; Figures 7b and 7c), which are modulated by distinct PV transformation processes. On average, diapycnal mixing attenuates these anomalies, through a net loss of EUC volume to the lower layer. Within the ensemble of other processes, isopycnal mixing generally acts to also buffer the anomalies by mixing local $Q \approx f$ water with the $Q_{EUC} \approx 0$ water of the EUC bifurcating branches. The local effects of friction on PV depend on the type of friction (bottom or lateral). The effect of bottom friction can, in principle, be predicted and depends on the direction of the current along the topography (Benthuysen & Thomas, 2012; D'Asaro, 1988; Gula et al., 2015, 2016). However, the direction of

the instantaneous currents varies so that both positive and negative anomalies are created (see the PV animation in Supporting Information S1). In addition, lateral friction, associated with horizontal viscosity operators, can also play a significant role and its sign cannot be easily predicted (Morel & McWilliams, 2001). Since all these isopycnal processes cannot be quantified in our simulation, we discuss their combined effects in δQ_{other}.

Averaged within our streamtubes, δQ_{mix} and δQ_{other} usually show the same sign, except for the Northern Hemisphere in WI. With the presence of São Tomé, δQ_{other} acts to strengthen the PV anomalies (Figures 7b and 7c). In WI, mixing has a stronger impact on the Northern Hemisphere anomalies, accounting for virtually 2/3 of the PV transformation ($\delta Q_{mix} = 7.2 \times 10^{-7}$ s^{-1} and $\delta Q_{other} = -3.5 \times 10^{-7}$ s^{-1}). In the Southern Hemisphere, diapycnal mixing is weaker and the buffering effect due to friction and isopycnal mixing is stronger. This leads to PV anomalies relative to the background planetary vorticity that are stronger in the Northern than in the Southern Hemisphere (Figure 7b). When the islands are removed, the EUC directly interacts with the continental slope and shelf waters, with both friction and mixing combined to attenuate the local PV anomalies. These anomalies in NI are weaker in the Northern Hemisphere than in the Southern Hemisphere, particularly because δQ_{mix} is larger in the Northern Hemisphere (Figure 7c). Also, the anomalies in the Northern Hemisphere of NI are weaker than those in WI, because δQ_{other} is stronger than, and has opposite sign to, that in WI (compare Fig 7b and Figure 7c). The effect of PV transformation on local PV anomalies is thus consistent with the asymmetry depicted in the mean PV (Figure 3) and potential enstrophy (Figure 5) distributions presented earlier.

Transformation of PV is key in setting the dynamics of the EUC in the Gulf of Guinea. Due to the presence of the islands and topography, both friction and diapycnal mixing must play a prominent role, since flow-topography interactions are known to induce strong mixing (e.g., Lueck & Mudge, 1997; Naveira Garabato et al., 2004) and introduce PV anomalies (e.g., Gula et al., 2019; Napolitano et al., 2020; Wenegrat et al., 2018). Assene et al. (2020) showed that isopycnal mixing also takes place during the rearranging of PV anomalies into eddies. Those diabatic processes, as well as diapycnal mixing, are generally parameterized in numerical models. Therefore, without rigorous quantitative budgets, the complete isolation of each process and where they occur could not be done in the simplified framework presented here. In this matter, the role of the islands (so as the difference between WI and NI) remains an open question due to their proximity with other sources of mixing and friction within the peculiar configuration of the Gulf of Guinea. Future studies are needed on this subject to quantify different processes and improve future numerical model parameterizations.

In our model, diapycnal mixing between adjacent layers points to an erosion of the salinity maximum (i.e., freshening) of the EUC, which can influence the local dynamics and the net transport of salt across the tropical Atlantic, motivating us to look closer at the EUC-island regional interaction. Due to high stratification between the EUC and the near-surface waters, we assume that the net diapycnal flux leaving the EUC ($\delta V < 0$) is primarily associated with mixing with the lower layer (defined between the 1,026.4 and 1,026.8 kg m^{-3} isopycnals). To understand how mixing occurs around the islands, we turn to salinity diagnostics in the lower layer of the EUC and diagnostics from a regional Lagrangian experiment.

4.2. The Salinity Imprint in the Lower Layer

In the eastern Gulf of Guinea, the low-PV, high-salinity tongue of the EUC along the Equator also presents a signature in deeper layers (e.g., Assene et al., 2020). This salty signature is strongest in the innermost portions of the gulf, where the EUC interacts with the gulf's islands, although the signal is also traceable within the westward-propagating mesoscale eddies (for details, see Figure 7d from Assene et al., 2020). In the near-surface layer, exchanges with the EUC are also expected (e.g., Da-Allada et al., 2017), but the EUC imprint in this layer is not as clear as it is in the lower layer (Figure 8) due to the upper layer dynamics. Thus, the following discussion focuses on the vertical exchanges between the EUC layer and the lower layer.

To qualitatively investigate the imbalance in the salt content depicted by $\lambda < 1$ (Equation 4) in the last section, we analyze the salinity distribution in the lower layer (defined in Section 4.1). Figure 8a shows the salinity vertically averaged within the lower layer in the WI simulation. We depict a weak eastward flow (using the same velocity scales as Figure 2), which represents the deeper end of the EUC and practically disappears east of 5°E. The salt signature from the EUC is faint along the flow, but drastically increases east of 5°E, forming a salty pool of $S > 35.6$ that stands out upstream of São Tomé. This relatively high-salinity area appears where the EUC is topographically forced to bifurcate. This suggests that vertical exchanges between the layers occur
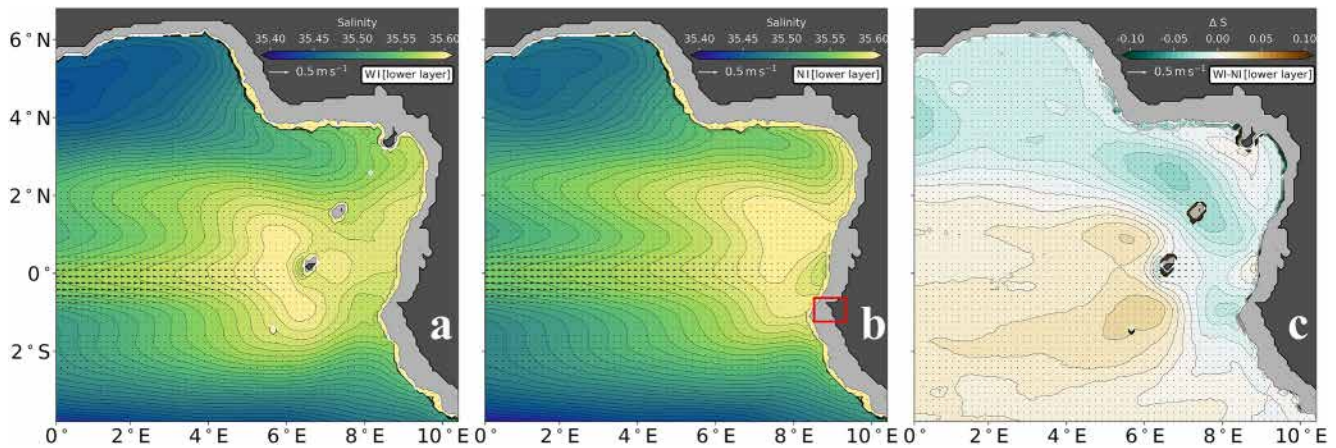
Figure 8. Mean Nucleus for European Modeling of the Ocean (NEMO) salinity below the Equatorial Undercurrent, vertically averaged within the lower layer (1,026.4–1,026.8 kg m^{-3}) for (a) the NEMO With Islands simulation, (b) the NEMO No Islands simulation, where the red rectangle highlights Cape Lopez (Gabon; 1°S, 8.5°E), and (c) the difference between WI and NI. Arrows represent the mean velocity within the layer.

upstream of and around the islands, where mixing tends to be greatly enhanced (Lueck & Mudge, 1997; Naveira Garabato et al., 2004; Nikurashin & Ferrari, 2010; Whalen et al., 2020), entraining lower-layer fresher waters into the EUC and maximum salinity waters from the EUC into the lower layer. Downstream of the island, other local maxima also appear (with salinity values slightly lower than the salty pool, e.g., at 7°E), possibly associated with a secondary diapycnal mixing region and isopycnal mixing between the salty pool and local waters due to mesoscale activity.

In the lower layer of NI (Figure 8b), the salty pool associated with mixing between the EUC and the lower layer also appears where the EUC bifurcates, in this case next to the continental slope. This is reflected in an overall negative ΔS anomaly in the innermost portions of the gulf also in the lower layer (Figure 8c; see also Figure 2c). Contrary to the EUC layer, in the lower layer the imprint of salinity is clearly asymmetric toward the Northern Hemisphere in NI, probably due to a prominent deeper extension of Cape Lopez (Gabon; 1°S, 8.5°E; Figure 8b) that might restrain the flow. The imprint associated with the early bifurcation due to São Tomé in Figure 8a is also depicted in Figure 8c by two positive anomalies north and southwest of the island, with a stronger positive anomaly extending from São Tomé westward along the south corridor, possibly due to the combination of island-induced mixing in WI and the southern branch partially blocked at Cape Lopez in NI.

To further investigate the changes in salinity derived from the interaction of the EUC with the Gulf of Guinea islands, we turn at last to a regional Lagrangian study case, focused on the fate of EUC waters around the islands.

4.3. The EUC Clash With São Tomé

To obtain a detailed view of the EUC bifurcation and tracer modification in the vicinity of São Tomé Island, we performed a particle tracking experiment with outputs of the WI simulation. We advected virtual drifters using Parcels v.2.2 framework (oceanparcels.org; Delandmeter & Sebille, 2019). Parcels provides a community based, adaptive, and computationally efficient Lagrangian simulator (cf., Delandmeter & Sebille, 2019; Lange & Sebille, 2017), extensively used for the computation of ocean particle trajectories (e.g., Van Sebille et al., 2021; access oceanparcels.org/#peerreviewedarticles for other examples).

In the Gulf of Guinea, we seeded particles within the EUC core layer, dispensed evenly in a blob spanning 0.5°S–0.5°N and 3–3.8°E. The blob was limited by EUC thresholds of salinity ($\geq$35.9), velocity ($\geq$0.5 m s^{-1}), and PV ($|Q| \leq 0.4 \times 10^{-5}$ s^{-1}), with particle density increased until reaching an approximately common solution. The 864 particles released on 20 September 2007—before the strong eddy activity observed in Figure 6b—were advected by the model flow during 40 days, recording latitude, longitude, depth, and salinity along their trajectories. We time-stepped an evolution equation for $X(t)$, where X is the three-dimensional position of the particle at time t with a time-step $\delta t = 5$ min, using a 4th order Runge-Kutta integration scheme, which includes vertical velocity. To obtain the salinity diagnostics, we added the salinity fields to the Parcels JIT (just-in-time) particle
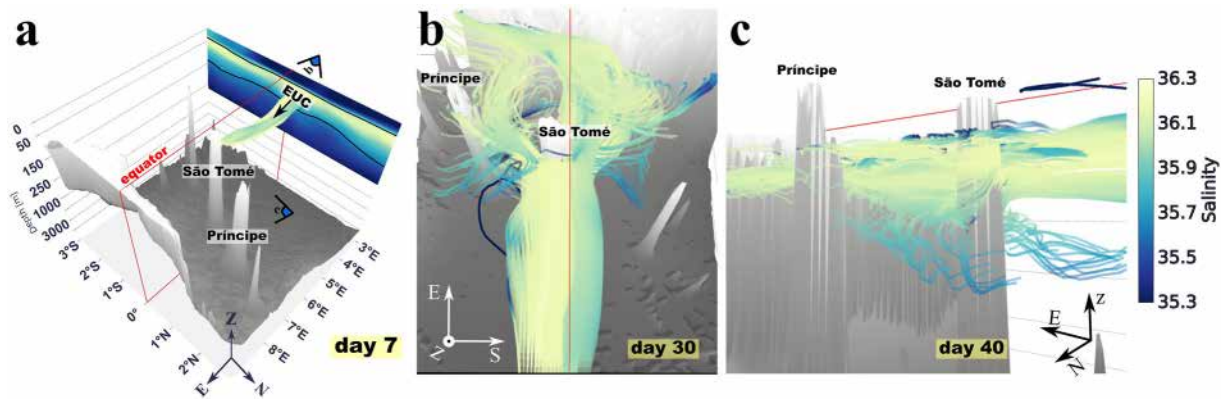
Figure 9. Snapshots from different angles for the trajectories in the Lagrangian simulation. Colors represent salinity, and lines represent individual trajectories from virtual floats deployed within the Equatorial Undercurrent (EUC) limits at 3°E, and then advected for 40 days. (a) 3D view (perspective from the African continent) of trajectories at day 7 of the Lagrangian simulation, with the arrow indicating the eastward EUC flow. A vertical section of salinity on day 1 shows the EUC layer, delimited by the 1,025.3 and 1,026.4 kg m^{-3} isopycnals (black lines). The blue semicircles tagged b and c indicate the viewer position for panels (b) and (c), respectively. (b) Trajectories highlighting the mesoscale activity associated with São Tomé and Príncipe Islands on day 30 (aerial view from 0°N, 3°E toward the continent). (c) Trajectories capturing the vertical displacements and salinity changes on day 40 (perspective from the bottom of the ocean at 1°N, 4°E toward the continent).

class, which already samples the 4D position of the particles (e.g., Lange & Sebille, 2017). Finally, we also added two extra kernel functions, one that deletes particles that go out of bounds and other to sample salinity values along the float trajectories (see Lange & Sebille, 2017, for the detailed definition of the kernels).

Different views of the simulated trajectories are displayed in Figure 9. Figure 9a shows a vertical section of salinity at 3°E (day 1), where the EUC isopycnals 1,025.3 and 1,026.4 kg m^{-3} delimits the high-salinity band of SMW and SACW. Particles released within the EUC traveled more than 300 km in about 7 days until reaching the vicinity of São Tomé. Moments before the impact (day 7), a snapshot of the trajectories captures the particles flowing with the EUC alongside the Equator from the deployment site at 3°E to immediately upstream of São Tomé Island at 6°E (Figure 9a). On the following days, the trajectories bifurcate while the EUC negotiates the island's topography. On day 30, an aerial west-to-east view (Figure 9b) displays the bifurcation and its associated mesoscale activity, particularly an anticyclonic meander in the Northern Hemisphere, developing in the lee of São Tomé, between this island and Príncipe Island. Figure 9b also captures the latitudinal spread downstream of the islands, as well as a few trajectories that veer to the west in both hemispheres, with salinity values lower than the initial values at the EUC. (Note that we have excluded trajectories with salinity changes greater than 1.5 due to interpolation errors too close to topography.) Finally, on the last day of the experiment, Figure 9c poses a view from below, focusing on particles that headed back west after interacting with the islands' topography. Interestingly, trajectories presented great changes in depth immediately upstream and while negotiating the island, with remarkable downwelling accompanied by (but not necessarily related to) a salinity decrease in the trajectories veering westward (Figure 9c). This intense downwelling upstream of São Tomé brings the EUC waters into the lower layer. Such downwelling events may also contribute to the salty pool observed in the lower layer (Figure 8). Also in Figure 9c, we depict upwelling particles that also freshen while navigating near São Tomé.

To better understand the fate of floats due to the interaction of the EUC with São Tomé, we retrieved quantitative diagnostics from the Lagrangian experiment. First, we defined a time t' relative to the float position with respect to São Tomé Island. When trajectories approach the island from the west (upstream), $t' = 0$ represents the day that the float was closest to São Tomé, being at least 10 km from the island and no more than 100 km away from it. Second, we re-indexed the trajectories by t' and selected the position at $t' = 30$ for particles that stayed at least within a 120-km-radius from the island. From the 864 particles deployed initially, 199 (23%) met the criteria above. For those particles, we observe changes in depth $Z' = Z(t') - Z(t' = -9)$ and salinity $S' = S(t') - S(t' = -9)$ through the probability density function (pdf) of these quantities binned within their values along trajectories (e.g., Van Sebille et al., 2018) for different times relative to São Tomé (Figure 10). In the following discussion, $Z' < 0$ represents sinking and $S' < 0$ represents freshening.

Particles carried by the EUC approached São Tomé with mean depth and salinity values typical of this eastward flow, 96 ± 19 m and 36.10 ± 0.09, respectively. In median values, 1 day before reaching the island, ~80% of the
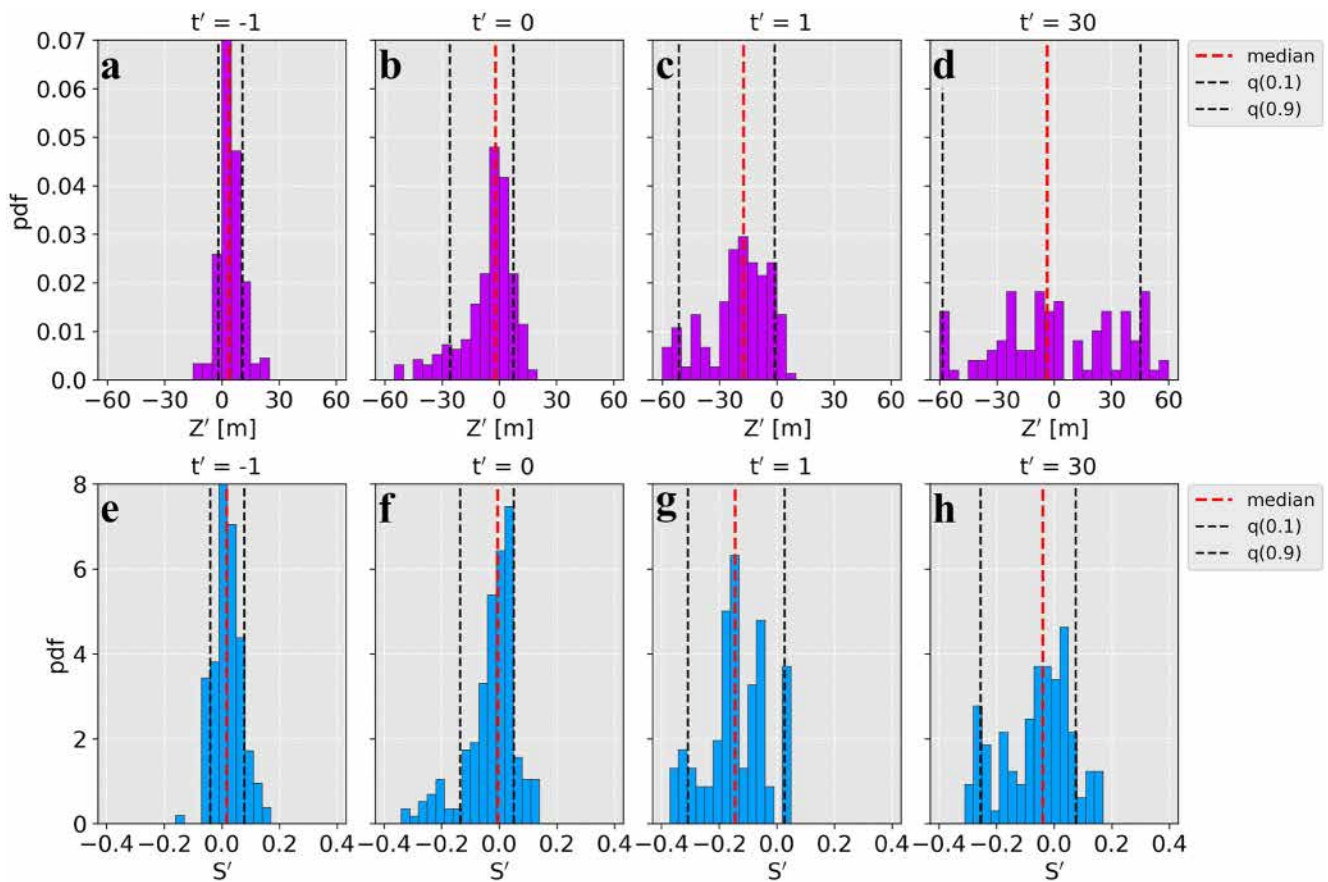
Figure 10. Probability density function for changes in depth and salinity along 40 days of particle trajectory, relative to the Equatorial Undercurrent encounter with São Tomé at $t' = 0$. (a–d) Pdf of the depth changes (Z') in different times t' relative to São Tomé. (e–h) Pdf of the salinity changes (S') in different times t' relative to São Tomé. Red dashed lines represent the median value of the distribution and black dashed lines represent its 0.1 and 0.9 quantiles. For (a) and (e), the y-axis is limited for better visualization, with maximum pdf values of 0.09 and 11.42 for Z' and S', respectively. $Z' < 0$ indicates sinking and $S' < 0$ indicates freshening.

particles showed only slight displacements (no more than ± 4 m) and virtually the same salinity ($< \pm 0.05$) from the EUC depth and salinity at $t' = -9$ (Figures 10a and 10e). At the last position upstream of the island ($t' = 0$), the tail in the pdf and the shift of the 0.1 quantile hints at particles starting to sink and lose salt when approaching São Tomé (Figures 10b and 10f). Immediately downstream of the island, strong downwelling at $t' = 1$ sinks 90% of the particles (Figure 10c), with median values of 17 m and 10% of particles sinking >50 m below Z_0. As does sinking, freshening also increases from $t' = 0$ to $t' = 1$, with $\sim 90\%$ of the particles presenting a negative anomaly and overall S' median values of -0.15. Further downstream, particles undergo strong changes in Z' before stabilizing from $t' \sim 10$ (not shown). At the end of the experiment ($t' = 30$), the Z' distribution has drastically changed, with original EUC particles vertically moving $Z' = \pm 60$ m (Figure 10d). From the S' distribution, we observe an overall freshening of the EUC after the interaction with São Tomé: if on the one hand the upper 10% of the distribution (0.9 quantile) has not moved from $t' = -1$ to $t' = 30$ (~ 0.07), on the other hand the lower limit (0.1 quantile) decreased from -0.04 to -0.25, with a net median decrease of 0.06 (Figure 10h).

The initial EUC-island encounter favors downwelling, also triggering mesoscale activity and mixing. Downstream of the island, both downwelling and upwelling seems to occur. While vertical advection is directly associated with changes in Z', mixing that changes S' can also affect the particle's depth by generating density anomalies, which will trigger vertical motions toward equilibrium. Since particles simultaneously sink and lose salt (Figures 10b and 10g; see also Qu et al., 2013), it is probable that mixing with the lower layer occurs, with the stabilization of trajectories at different depth levels pointing to density changes. Downwelling and mixing of maximum salinity water also plays a role in the formation and transport of the Pacific EUC waters, dampening the "source waters" signal (e.g., Qu et al., 2013) and in the freshening of the Red Sea Overflow Water in the Arabian Sea (e.g., Menezes, 2021). Using a particle-tracking approach to infer changes in passive tracers can be sensitive to time

sampling and spatial interpolation. Therefore, we encourage future sensitivity studies addressing the role of particle-tracking numerical schemes in the potential non-conservation of passive tracers in the absence of mixing.

Although comprising a particular event over 40 days, our Lagrangian study case can be considered representative of the model dynamics near the islands within the EUC layer, that is, the vertical motions highlighted in Figure 9c and discussed above are also represented in the model vertical velocity w (Figure 11). In Figure 11, we first calculate the divergence field of the EUC-layer horizontal velocities, $\nabla_H \cdot \mathbf{u} = \partial_x u + \partial_y v$, then obtaining w within regions of strong convergence and divergence (For the mean divergence curves displayed in Figure 11a, we used the time-mean horizontal velocity.). The EUC-layer mean vertical velocity w shows the greatest values ($\pm 6 \times 10^{-6}$ m s^{-1}) near São Tomé (Figure 11a). West (upstream) of the island, a large downwelling region with negative vertical velocity appears, associated with strongest *mean* convergence (-1×10^{-6} s^{-1}) where the EUC decelerates approaching São Tomé. Downstream, positive mean vertical velocity dominates, particularly on the sides of the island, where a divergence zone is created between the EUC branches flowing north and southward and the EUC (Figure 11a). In glider sections around the Galápagos, Jakoboski et al. (2020) reported weak vertical velocities at the Pacific EUC layer. But in the Galápagos case, a vertical spread in the bifurcating branches compensates for convergence when the EUC approaches the island, resulting in (integrated) upwelling (Jakoboski et al., 2020).

Time-averaging w in the domain, and remembering that the EUC undergoes seasonal and higher-frequency variability when interacting with the islands, fluctuations of the vertical velocity yielded standard deviations much greater than the mean for Figure 11a. To get a clearer picture of the dynamics due to the EUC interaction with São Tomé, we evaluate w within curves of strong convergence and divergence (i.e., below and above the 0.05 and 0.95 quantiles of the divergence field distribution, respectively) that changed daily within the limits of Figure 11a. While convergence is generally associated with the EUC approaching the islands, divergence regions are created between the island and the EUC branches that veer northwest and southwestward. Figures 11b–11e show the distribution and time series of the 7-day filtered model vertical velocity, capturing persistent downwelling upstream and upwelling downstream of São Tomé in the later half of every year. Within the EUC layer, both upwelling and downwelling occur at each region, in a "vertical bifurcation" pattern similar to that inferred by Karnauskas et al. (2010) for the Pacific EUC encounter with the Galápagos. Nevertheless, averaging w within the EUC layer, downwelling occurs >99% of the time in the vertical velocity series within convergence regions (Figures 11b and 11d), with $w = -31.3 \times 10^{-6} \pm 20.5 \times 10^{-6}$ m s^{-1}. The downwelling also reflects the seasonal and higher-frequency variability of the EUC, with strong downwelling opposing eddy-formation periods (compare the peaks between Figures 11 and 6b). The contrary occurs for divergence regions: on average, upwelling dominates >99% of the time series, with similar magnitude ($33.4 \times 10^{-6} \pm 15.0 \times 10^{-6}$ m s^{-1}) and peaks (visually) correlated with strong downwelling periods (Figures 11c and 11e).

We here remind the reader that this analysis represent diagnostics from a numerical simulation which, like every other model, presents strengths and weaknesses. If on the one hand the staircase bathymetry of our simulation allows the representation of steep volcanic islands (which would have been severely smoothed in a sigma-coordinate model at this resolution), on the other hand this may introduce numerical uncertainties in the vertical velocity and modeling of the bottom friction compared with sigma-coordinate models. However, by comparing regions next to and far from the islands, we reasoned that potential numerical w uncertainties introduced by boundary effects would not likely alter our conclusions.

To conclude, we showed that the EUC slowing down upstream of São Tomé creates convergence regions that cause sustained downwelling. Downstream of the island, these waters upwell within the EUC layer. Strong vertical velocities modulated by the EUC seasonal dynamics (Figure 11) may also have an impact on eddy formation and consequently on the net fluxes between the eastern and western tropical Atlantic. Regions of strong vertical motions are also generally indicative of mixing, since important changes in salinity (Figure 10f) modify the particles' density, forcing them to readjust to depth levels as a function of an evolving density.

5. Final Remarks

Observations that capture the EUC upstream of and aligned with São Tomé Island indicate an inevitable collision between this strong current and the island's topography. Using two NEMO simulations that differ only in the presence versus absence of the islands in the Gulf of Guinea, we show that the EUC bifurcates earlier at São
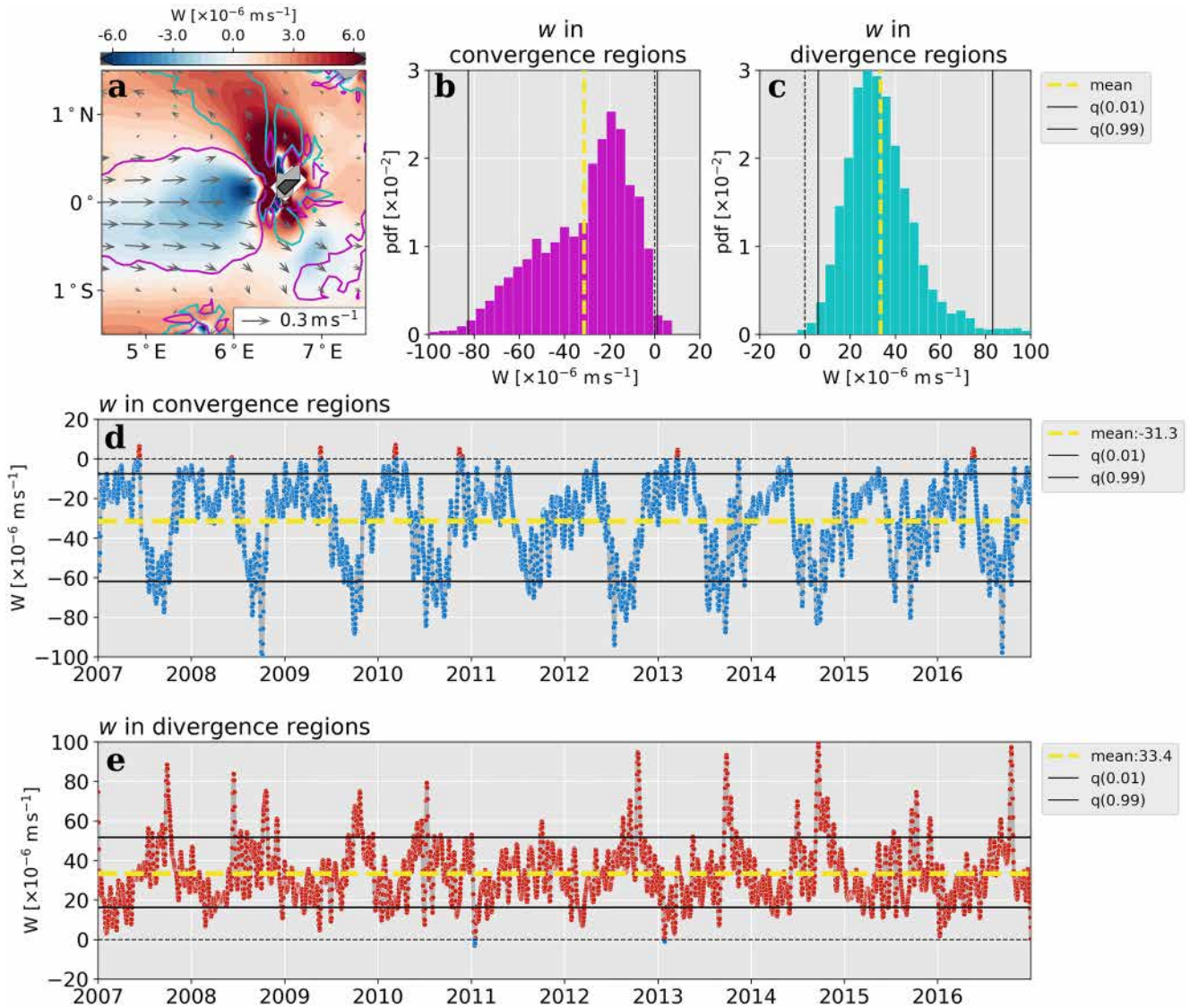
Figure 11. Nucleus for European Modeling of the Ocean vertical velocity vertically averaged within the Equatorial Undercurrent layer. (a) Time-mean horizontal distribution of the vertical velocity (colors), with arrows representing the layer's mean horizontal velocity; the magenta and cyan curves are obtained from the time-mean horizontal velocity as $\partial_x \overline{u} + \partial_y \overline{v}$ and delimit (with values $\pm 10^{-6}\,s^{-1}$) the mean convergence and divergence regions around São Tomé Island, respectively. In (b–e), vertical velocities are obtained within daily strong convergence/divergence contours (i.e., below and above the 0.05 and 0.95 quantiles of the divergence field distribution, respectively), displayed as: (b, c) pdf of the 7-day-filtered model vertical velocities within the convergence and divergence regions. (d, e) time series of the 7-day-filtered model vertical velocities within the convergence and divergence regions. Positive values (red) indicate upward vertical velocities, while negative values (blue) indicate downward vertical velocities.

Tomé when the island is present, generating mesoscale activity downstream and mesoscale anticyclonic eddies that propagate westward. This encounter is the main driver of subsurface flow-topography interactions in the Gulf of Guinea, which affect the region's meso-to-large scale circulation and fuels the inverse energy cascade.

In the meso-to-large-scale circulation, anticyclonic eddies generated at the EUC bifurcation carry salinity and PV through zonal corridors into the western tropical Atlantic, bringing anomalies that drive the large-scale circulation and tracer patterns. The eddy-formation process involves not only the EUC branches crossing the planetary vorticity gradient and developing local anticyclonic PV anomalies, but also transformation of PV through diapycnal mixing and friction and isopycnal mixing, which combined will act to attenuate the anomalies. Acting as a physical barrier, São Tomé is directly responsible for forcing the EUC bifurcation at ∼6.5°E, causing a large spread of high-salinity and low-PV waters downstream of the islands. The islands also prevent the EUC waters from reaching the innermost portions of the gulf, for instance the region around Bioko Island. The EUC-São

Tomé interactions present a seasonal and interannual variability that is reflected in an equatorial asymmetry in the strength and formation rate of the westward-propagating eddies. In a nutshell, a weaker EUC hinders eddy formation during seasonal equatorial upwelling whereas a strong EUC boost the number and strength of eddies formed, with seasonal and interannual meridional displacements northward potentially adding to this increase.

Virtual float trajectories in a regional Lagrangian experiment generally show downwelling as the EUC approaches São Tomé. Downstream of the islands, intense mixing drives salinity changes. At the same time, particles move up and down the water column, stabilizing at new depth levels due to density changes, with a net downwelling and freshening of the EUC waters. The brief experiment is backed up by the model vertical velocities, which show downwelling hotspots associated with convergence of the EUC upstream of São Tomé, followed by downstream strong divergence-upwelling sites on the flanks of the island.

To advance in the understanding of the EUC interaction with the islands of the Gulf of Guinea, several topics addressed in this study demand further attention, for example, the thorough assessment of the spatial and timescales of the EUC variability near its termination site, the mechanisms controlling the generation of PV anomalies, the relation between vertical velocities and eddy formation, and how different models reproduce the dynamics adjacent to the islands. In addition, future work will need to further explore the vertical structure of vertical velocities within the EUC layer and the biogeochemical impacts of flow-topography interactions in the Gulf of Guinea. The EUC transports high oxygen and low nutrient waters, and its interaction with the islands forces upwelling and downwelling, as well as redistribution of these waters by vertical advection and mixing processes through meso- and submesoscale dynamics. All these processes embedded in a background of nutrient-rich coastal water and low-oxygen deeper layers are likely to impact the productivity and oxygen minimum zone in the Gulf of Guinea.

Data Availability Statement

The French PIRATA cruises and the Enhanced PIRATA data set are publicly available at https://www.seanoe.org/data/00335/44635/ and https://www.pmel.noaa.gov/tao/drupal/disdel/, respectively. The processed model outputs used in this study can be distributed on demand. Animation within the Supporting Information S1 can be obtained at https://jmp.sh/QOM2NF2.

References

Alory, G., Da-Allada, C. Y., Djakouré, S., Dadou, I., Jouanno, J., & Loemba, D. P. (2021). Coastal upwelling limitation by onshore geostrophic flow in the Gulf of Guinea around the Niger River plume. *Frontiers in Marine Science*, 7, 1116. https://doi.org/10.3389/fmars.2020.607216

Argo (2020). *Argo float data and metadata from global data assembly centre (Argo GDAC)*. SEANOE. https://doi.org/10.17882/42182%2376230

Arístegui, J., Sangrá, P., Hernández-León, S., Cantón, M., Hernández-Guerra, A., & Kerling, J. L. (1994). Island-induced eddies in the Canary Islands. *Deep Sea Research Part I: Oceanographic Research Papers*, 41(10), 1509–1525. https://doi.org/10.1016/0967-0637(94)90058-2

Assene, F., Morel, Y., Delpech, A., Aguedjou, M., Jouanno, J., Cravatte, S., et al. (2020). From mixing to the large scale circulation: How the inverse cascade is involved in the formation of the subsurface currents in the Gulf of Guinea. *Fluids*, 5(3), 147. https://doi.org/10.3390/fluids5030147

Awo, F. M., Alory, G., Da-Allada, C. Y., Delcroix, T., Jouanno, J., Kestenare, E., & Baloïtcha, E. (2018). Sea surface salinity signature of the tropical Atlantic interannual climatic modes. *Journal of Geophysical Research: Oceans*, 123(10), 7420–7437. https://doi.org/10.1029/2018JC013837

Bachèlery, M. L., Illig, S., & Dadou, I. (2016). Interannual variability in the South-East Atlantic Ocean, focusing on the Benguela upwelling system: Remote versus local forcing. *Journal of Geophysical Research: Oceans*, 121(1), 284–310. https://doi.org/10.1002/2015JC011168

Benthuysen, J., & Thomas, L. N. (2012). Friction and diapycnal mixing at a slope: Boundary control of potential vorticity. *Journal of Physical Oceanography*, 42(9), 1509–1523. https://doi.org/10.1175/JPO-D-11-0130.1

Blanke, B., Arhan, M., Lazar, A., & Prévost, G. (2002). A Lagrangian numerical investigation of the origins and fates of the salinity maximum water in the Atlantic. *Journal of Geophysical Research*, 107(C10), 27. https://doi.org/10.1029/2002JC001318

Blanke, B., & Delecluse, P. (1993). Variability of the Tropical Atlantic Ocean simulated by a general circulation model with two different mixed-layer physics. *Journal of Physical Oceanography*, 23(7), 1363–1388. https://doi.org/10.1175/1520-0485(1993)023⟨1363:VOTTAO⟩2.0.CO;2

Blayo, E., & Debreu, L. (1999). Adaptive mesh refinement for finite-difference ocean models: First experiments. *Journal of Physical Oceanography*, 29(6), 1239–1250. https://doi.org/10.1175/1520-0485(1999)029⟨1239:AMRFFD⟩2.0.CO;2

Bourlès, B., Araujo, M., McPhaden, M. J., Brandt, P., Foltz, G. R., Lumpkin, R., et al. (2019). PIRATA: A sustained observing system for tropical Atlantic climate research and forecasting. *Earth and Space Science*, 6(4), 577–616. https://doi.org/10.1029/2018EA000428

Bourlès, B., Herbert, G., Rousselot, P., & Grelet, J. (2018). *French PIRATA cruises: S-ADCP data*. SEANOE. https://doi.org/10.17882/44635

Bourlès, B., Lumpkin, R., McPhaden, M. J., Hernandez, F., Nobre, P., Campos, E., et al. (2008). The PIRATA program: History, accomplishments, and future directions. *Bulletin of the American Meteorological Society*, 89(8), 1111–1126. https://doi.org/10.1175/2008BAMS2462.1

Brandt, P., Funk, A., Hormann, V., Dengler, M., Greatbatch, R. J., & Toole, J. M. (2011). Interannual atmospheric variability forced by the deep equatorial Atlantic Ocean. *Nature*, 473(7348), 497–500. https://doi.org/10.1038/nature10013

Brandt, P., Funk, A., Tantet, A., Johns, W. E., & Fischer, J. (2014). The Equatorial Undercurrent in the central Atlantic and its relation to tropical Atlantic variability. *Climate Dynamics*, 43(11), 2985–2997. https://doi.org/10.1007/s00382-014-2061-4

Brandt, P., Hahn, J., Schmidtko, S., Tuchen, F. P., Kopte, R., Kiko, R., et al. (2021). Atlantic Equatorial Undercurrent intensification counteracts warming-induced deoxygenation. *Nature Geoscience*, *14*(5), 278–282. https://doi.org/10.1038/s41561-021-00716-1

Brandt, P., Schott, F. A., Provost, C., Kartavtseff, A., Hormann, V., Bourlès, B., & Fischer, J. (2006). Circulation in the central equatorial Atlantic: Mean and intraseasonal to seasonal variability. *Geophysical Research Letters*, *33*(7), L07609. https://doi.org/10.1029/2005GL025498

Bretherton, F. P., & Haidvogel, D. B. (1976). Two-dimensional turbulence above topography. *Journal of Fluid Mechanics*, *78*(1), 129–154. https://doi.org/10.1017/S002211207600236X

Cane, M. A., & Moore, D. W. (1981). A note on low-frequency equatorial basin modes. *Journal of Physical Oceanography*, *11*(11), 1578–1584. https://doi.org/10.1175/1520-0485(1981)011⟨1578:ANOLFE⟩2.0.CO;2

Chang, P., Zhang, R., Hazeleger, W., Wen, C., Wan, X., Ji, L., et al. (2008). Oceanic link between abrupt changes in the North Atlantic Ocean and the African monsoon. *Nature Geoscience*, *1*(7), 444–448. https://doi.org/10.1038/ngeo218

Charney, J. G. (1971). Geostrophic turbulence. *Journal of the Atmospheric Sciences*, *28*(6), 1087–1095. https://doi.org/10.1175/1520-0469(1971)028⟨1087:GT⟩2.0.CO;2

Copernicus Climate Change Service, C. (2017). ERA5: Fifth generation of ECMWF atmospheric reanalyses of the global climate. Copernicus Climate Change Service Climate Data Store (CDS). Documentation May 2019. Retrieved from https://cds.climate.copernicus.eu/cdsapp%23%21/home

D'Asaro, E. A. (1988). Generation of submesoscale vortices: A new mechanism. *Journal of Geophysical Research*, *93*(C6), 6685–6693. https://doi.org/10.1029/JC093iC06p06685

Da-Allada, C. Y., Jouanno, J., Gaillard, F., Kolodziejczyk, N., Maes, C., Reul, N., & Bourlès, B. (2017). Importance of the Equatorial Undercurrent on the sea surface salinity in the eastern equatorial Atlantic in boreal spring. *Journal of Geophysical Research: Oceans*, *122*(1), 521–538. https://doi.org/10.1002/2016JC012342

Delandmeter, P., & Sebille, E. v. (2019). The parcels v2.0 Lagrangian framework: New field interpolation schemes. *Geoscientific Model Development*, *12*(8), 3571–3584. https://doi.org/10.5194/gmd-12-3571-2019

Delpech, A., Cravatte, S., Marin, F., Morel, Y., Gronchi, E., & Kestenare, E. (2020). Observed tracer fields structuration by middepth zonal jets in the tropical Pacific. *Journal of Physical Oceanography*, *50*(2), 281–304. https://doi.org/10.1175/JPO-D-19-0132.1

ETOPO2. (2001). *National Geophysical Data Center, NESDIS, NOAA, U.S. Department of Commerce. Global 2 Arc-Minute Ocean Depth and Land Elevation from the US National Geophysical Data Center (NGDC)*. Research Data Archive at the National Center for Atmospheric Research, Computational and Information Systems Laboratory. https://doi.org/10.5065/D6668B75

Ferry, N., Parent, L., Garric, G., Bricaud, C., Testut, C. E., Le Galloudec, O., et al. (2012). GLORYS2V1 global ocean reanalysis of the altimetric era (1992–2009) at mesoscale. In *Mercator Ocean–Quarterly Newsletter* (Vol. 44).

Fofonoff, N., & Montgomery, R. (1955). The Equatorial Undercurrent in the light of the vorticity equation. *Tellus*, *7*(4), 518–521. https://doi.org/10.3402/tellusa.v7i4.8910

Foltz, G. R., Brandt, P., Richter, I., Rodríguez-Fonseca, B., Hernandez, F., Dengler, M., et al. (2019). The tropical Atlantic observing system. *Frontiers in Marine Science*, *6*, 206. https://doi.org/10.3389/fmars.2019.00206

Foltz, G. R., Grodsky, S. A., Carton, J. A., & McPhaden, M. J. (2004). Seasonal salt budget of the northwestern tropical Atlantic Ocean along 38 W. *Journal of Geophysical Research*, *109*(C3), C03052. https://doi.org/10.1029/2003JC002111

Foltz, G. R., Schmid, C., & Lumpkin, R. (2018). An enhanced PIRATA dataset for tropical Atlantic Ocean–Atmosphere research. *Journal of Climate*, *31*(4), 1499–1524. https://doi.org/10.1175/JCLI-D-16-0816.1

Goes, M., Molinari, R., Silveira, I. C. A., & Wainer, I. (2005). Retroflections of the North Brazil current during February 2002. *Deep Sea Research Part I: Oceanographic Research Papers*, *52*(4), 647–667. https://doi.org/10.1016/j.dsr.2004.10.010

Gouriou, Y., & Reverdin, G. (1992). Isopycnal and diapycnal circulation of the upper equatorial Atlantic Ocean in 1983–1984. *Journal of Geophysical Research*, *97*(C3), 3543–3572. https://doi.org/10.1029/91{JC}02935

Gula, J., Blacic, T. M., & Todd, R. E. (2019). Submesoscale coherent vortices in the gulf stream. *Geophysical Research Letters*, *46*(5), 2704–2714. https://doi.org/10.1029/2019GL081919

Gula, J., Molemaker, M., & McWilliams, J. (2015). Topographic vorticity generation, submesoscale instability and vortex street formation in the Gulf Stream. *Geophysical Research Letters*, *42*(10), 4054–4062. https://doi.org/10.1002/2015GL063731

Gula, J., Molemaker, M., & McWilliams, J. (2016). Topographic generation of submesoscale centrifugal instability and energy dissipation. *Nature Communications*, *7*(1), 12811. https://doi.org/10.1038/ncomms12811

Haynes, P. H., & McIntyre, M. E. (1987). On the evolution of vorticity and potential vorticity in the presence of diabatic heating and frictional or other forces. *Journal of the Atmospheric Sciences*, *44*(5), 828–841. https://doi.org/10.1175/1520-0469(1987)044⟨0828:OTEOVA⟩2.0.CO;2

Hazeleger, W., de Vries, P., & Friocourt, Y. (2003). Sources of the equatorial undercurrent in the Atlantic in a high-resolution ocean model. *Journal of Physical Oceanography*, *33*(4), 677–693. https://doi.org/10.1175/1520-0485(2003)33⟨677:SOTEUI⟩2.0.CO;2

Herbert, G., Bourlès, B., Penven, P., & Grelet, J. (2016). New insights on the upper layer circulation north of the Gulf of Guinea. *Journal of Geophysical Research: Oceans*, *121*(9), 6793–6815. https://doi.org/10.1002/2016JC011959

Herbert, G., Kermabon, C., Grelet, J., & Bourles, B. (2015). French PIRATA Cruises S-ADCP Data Processing (Computer Software Manual No. 52). Retrieved from https://archimer.ifremer.fr/doc/00272/38320/36561.pdf

Hormann, V., & Brandt, P. (2009). Upper equatorial Atlantic variability during 2002 and 2005 associated with equatorial kelvin waves. *Journal of Geophysical Research*, *114*(C3), C03007. https://doi.org/10.1029/2008JC005101

Hoskins, B. J., McIntyre, M. E., & Robertson, A. W. (1985). On the use and significance of isentropic potential vorticity maps. *Quarterly Journal of the Royal Meteorological Society*, *111*(470), 877–946. https://doi.org/10.1002/qj.49711147002

Houndegnonto, O., Kolodziejczyk, N., Maes, C., Bourlès, B., Da-Allada, C., & Reul, N. (2021). Seasonal variability of freshwater plumes in the Eastern Gulf of Guinea as inferred from satellite measurements. *Journal of Geophysical Research: Oceans*, *126*(5), e2020JC017041. https://doi.org/10.1029/2020JC017041

Illig, S., & Bachèlery, M.-L. (2019). Propagation of subseasonal equatorially-forced coastal trapped waves down to the Benguela upwelling system. *Scientific Reports*, *9*(1), 1–10. https://doi.org/10.1038/s41598-019-41847-1

Jakoboski, J., Todd, R. E., Owens, W. B., Karnauskas, K. B., & Rudnick, D. L. (2020). Bifurcation and upwelling of the equatorial undercurrent west of the Galápagos Archipelago. *Journal of Physical Oceanography*, *50*(4), 887–905. https://doi.org/10.1175/JPO-D-19-0110.1

Johns, W. E., Brandt, P., Bourlès, B., Tantet, A., Papapostolou, A., & Houk, A. (2014). Zonal structure and seasonal variability of the Atlantic equatorial undercurrent. *Climate Dynamics*, *43*(11), 3047–3069. https://doi.org/10.1007/s00382-014-2136-2

Johnson, G. C., Sloyan, B. M., Kessler, W. S., & McTaggart, K. E. (2002). Direct measurements of upper ocean currents and water properties across the tropical Pacific during the 1990s. *Progress in Oceanography*, *52*(1), 31–61. https://doi.org/10.1016/S0079-6611(02)00021-6

Jouanno, J., & Capet, X. (2020). Connecting flow–topography interactions, vorticity balance, baroclinic instability and transport in the southern ocean: The case of an idealized storm track. *Ocean Science*, *16*(5), 1207–1223. https://doi.org/10.5194/os-16-1207-2020

Jouanno, J., Marin, F., du Penhoat, Y., & Molines, J.-M. (2013). Intraseasonal modulation of the surface cooling in the Gulf of Guinea. *Journal of Physical Oceanography*, *43*(2), 382–401. https://doi.org/10.1175/JPO-D-12-053.1

Jouanno, J., Marin, F., Du Penhoat, Y., Molines, J.-M., & Sheinbaum, J. (2011). Seasonal modes of surface cooling in the Gulf of Guinea. *Journal of Physical Oceanography*, *41*(7), 1408–1416. https://doi.org/10.1175/JPO-D-11-031.1

Jouanno, J., Marin, F., Du Penhoat, Y., Sheinbaum, J., & Molines, J.-M. (2011). Seasonal heat balance in the upper 100 m of the equatorial Atlantic Ocean. *Journal of Geophysical Research*, *116*(C9), C09003. https://doi.org/10.1029/2010JC006912

Karnauskas, K. B., Murtugudde, R., & Busalacchi, A. J. (2007). The effect of the Galápagos Islands on the Equatorial Pacific cold tongue. *Journal of Physical Oceanography*, *37*(5), 1266–1281. https://doi.org/10.1175/JPO3048.1

Karnauskas, K. B., Murtugudde, R., & Busalacchi, A. J. (2008). The effect of the Galápagos Islands on ENSO in forced ocean and hybrid coupled models. *Journal of Physical Oceanography*, *38*(11), 2519–2534. https://doi.org/10.1175/2008JPO3848.1

Karnauskas, K. B., Murtugudde, R., & Busalacchi, A. J. (2010). Observing the Galápagos–EUC interaction: Insights and challenges. *Journal of Physical Oceanography*, *40*(12), 2768–2777. https://doi.org/10.1175/2010JPO4461.1

Kolodziejczyk, N., Bourlès, B., Marin, F., Grelet, J., & Chuchla, R. (2009). Seasonal variability of the Equatorial Undercurrent at 10W as inferred from recent in situ observations. *Journal of Geophysical Research*, *114*(C6), C06014. https://doi.org/10.1029/2008JC004976

Kolodziejczyk, N., Marin, F., Bourlès, B., Gouriou, Y., & Berger, H. (2014). Seasonal variability of the Equatorial Undercurrent termination and associated salinity maximum in the Gulf of Guinea. *Climate Dynamics*, *43*(11), 3025–3046. https://doi.org/10.1007/s00382-014-2107-7

Lange, M., & Sebille, E. V. (2017). Parcels v0.9: Prototyping a Lagrangian ocean analysis framework for the petascale age. *Geoscientific Model Development*, *10*(11), 4175–4186. https://doi.org/10.5194/gmd-10-4175-2017

Large, W., & Yeager, S. (2009). The global climatology of an interannually varying air-sea flux data set. *Climate Dynamics*, *33*(2–3), 341–364. https://doi.org/10.1007/s00382-008-0441-3

Li, Q., Sun, L., & Xu, C. (2018). The lateral eddy viscosity derived from the decay of oceanic mesoscale eddies. *Open Journal of Marine Science*, *8*(01), 152–172. https://doi.org/10.4236/ojms.2018.81008

Lueck, R. G., & Mudge, T. D. (1997). Topographically induced mixing around a shallow seamount. *Science*, *276*(5320), 1831–1833. https://doi.org/10.1126/science.276.5320.1831

Madec, G., & The NEMO Team. (2016). NEMO ocean engine (Computer Software Manual No. 27). *Zenodo*. https://doi.org/10.5281/zenodo.1464816

McCreary, J. P., & Yu, Z. (1992). Equatorial dynamics in a 2½-layer model. *Progress in Oceanography*, *29*(1), 61–132. https://doi.org/10.1016/0079-6611(92)90003-i

Mémery, L., Arhan, M., Alvarez-Salgado, X., Messias, M.-J., Mercier, H., Castro, C., & Rios, A. (2000). The water masses along the western boundary of the south and equatorial Atlantic. *Progress in Oceanography*, *47*(1), 69–98. https://doi.org/10.1016/S0079-6611(00)00032-X

Ménesguen, C., Hua, B. L., Fruman, M. D., & Schopp, R. (2009). Dynamics of the combined extra-equatorial and equatorial deep jets in the Atlantic. *Journal of Marine Research*, *67*(3), 323–346. https://doi.org/10.1357/002224009789954766

Menezes, V. V. (2021). Advective pathways and transit times of the Red Sea Overflow Water in the Arabian Sea from Lagrangian simulations. *Progress in Oceanography*, *199*, 102697. https://doi.org/10.1016/j.pocean.2021.102697

Metcalf, W., Voorhis, A., & Stalcup, M. (1962). The Atlantic equatorial undercurrent. *Journal of Geophysical Research*, *67*(6), 2499–2508. https://doi.org/10.1029/JZ067i006p02499

Montes, I., Colas, F., Capet, X., & Schneider, W. (2010). On the pathways of the equatorial subsurface currents in the eastern equatorial Pacific and their contributions to the Peru-Chile undercurrent. *Journal of Geophysical Research*, *115*(C9), C09003. https://doi.org/10.1029/2009JC005710

Morel, Y., Gula, J., & Ponte, A. (2019). Potential vorticity diagnostics based on balances between volume integral and boundary conditions. *Ocean Modelling*, *138*, 23–35. https://doi.org/10.1016/j.ocemod.2019.04.004

Morel, Y., & McWilliams, J. (2001). Effects of isopycnal and diapycnal mixing on the stability of oceanic currents. *Journal of Physical Oceanography*, *31*(8), 2280–2296. https://doi.org/10.1175/1520-0485(2001)031⟨2280:EOIADM⟩2.0.CO;2

Müller, P. (2006). *The equations of oceanic motions*. Cambridge University Press.

Napolitano, D. C., Silveira, I. C. A., Tandon, A., & Calil, P. H. R. (2020). Submesoscale phenomena due to the Brazil current crossing of the Vitória-Trindade ridge. *Journal of Geophysical Research: Oceans*, *126*(1), e2020JC016731. https://doi.org/10.1029/2020JC016731

Naveira Garabato, A. C., Polzin, K. L., King, B. A., Heywood, K. J., & Visbeck, M. (2004). Widespread intense turbulent mixing in the Southern Ocean. *Science*, *303*(5655), 210–213. https://doi.org/10.1126/science.1090929

Nikurashin, M., & Ferrari, R. (2010). Radiation and dissipation of internal waves generated by geostrophic motions impinging on small-scale topography: Application to the Southern Ocean. *Journal of Physical Oceanography*, *40*(9), 2025–2042. https://doi.org/10.1175/2010JPO4315.1

Pedlosky, J. (1987). An inertial theory of the Equatorial Undercurrent. *Journal of Physical Oceanography*, *17*(11), 1978–1985. https://doi.org/10.1175/1520-0485(1987)017⟨1978:AITOTE⟩2.0.CO;2

Pedlosky, J., & Spall, M. A. (2015). The interaction of an eastward-flowing current and an island: Sub- and supercritical flow. *Journal of Physical Oceanography*, *45*(11), 2806–2819. https://doi.org/10.1175/JPO-D-15-0061.1

Picaut, J. (1983). Propagation of the seasonal upwelling in the eastern Equatorial Atlantic. *Journal of Physical Oceanography*, *13*(1), 18–37. https://doi.org/10.1175/1520-0485(1983)013⟨0018:POTSUI⟩2.0.CO;2

Polo, I., Lazar, A., Rodriguez-Fonseca, B., & Arnault, S. (2008). Oceanic kelvin waves and tropical Atlantic intraseasonal variability: 1. Kelvin wave characterization. *Journal of Geophysical Research*, *113*(C7), C07009. https://doi.org/10.1029/2007JC004495

Qu, T., Gao, S., & Fine, R. A. (2013). Subduction of South Pacific tropical water and its equatorward pathways as shown by a simulated passive tracer. *Journal of Physical Oceanography*, *43*(8), 1551–1565. https://doi.org/10.1175/JPO-D-12-0180.1

Rabe, B., Schott, F. A., & Köhl, A. (2008). Mean circulation and variability of the tropical Atlantic during 1952–2001 in the GECCO assimilation fields. *Journal of Physical Oceanography*, *38*(1), 177–192. https://doi.org/10.1175/2007JPO3541.1

Rhines, P. B. (1986). Vorticity dynamics of the oceanic general circulation. *Annual Review of Fluid Mechanics*, *18*(1), 433–497. https://doi.org/10.1146/annurev.fl.18.010186.002245

Roemmich, D., & Gilson, J. (2009). The 2004–2008 mean and annual cycle of temperature, salinity, and steric height in the global ocean from the Argo Program. *Progress in Oceanography*, *82*(2), 81–100. https://doi.org/10.1016/j.pocean.2009.03.004

Sangrà, P., Pascual, A., Rodríguez-Santana, Á., Machín, F., Mason, E., McWilliams, J. C., et al. (2009). The Canary Eddy Corridor: A major pathway for long-lived eddies in the subtropical North Atlantic. *Deep Sea Research Part I: Oceanographic Research Papers*, *56*(12), 2100–2114. https://doi.org/10.1016/j.dsr.2009.08.008

Schott, F. A., Fischer, J., & Stramma, L. (1998). Transports and pathways of the upper-layer circulation in the western tropical Atlantic. *Journal of Physical Oceanography*, *28*(10), 1904–1928. https://doi.org/10.1175/1520-0485(1998)028⟨1904:TAPOTU⟩2.0.CO;2

Silveira, I. C. A., Brown, W. S., & Flierl, G. R. (2000). Dynamics of the North Brazil current retroflection region from the western tropical Atlantic experiment observations. *Journal of Geophysical Research*, *105*(C12), 28559–28583. https://doi.org/10.1029/2000JC900129

Snowden, D. P., & Molinari, R. L. (2003). Subtropical cells in the Atlantic Ocean: An observational summary. In *Elsevier oceanography series* (Vol. 68, pp. 287–312). Elsevier.

Stramma, L., & Schmidtko, S. (2021). Tropical deoxygenation sites revisited to investigate oxygen and nutrient trends. *Ocean Science*, *17*(3), 833–847. https://doi.org/10.5194/os-17-833-2021

Stramma, L., & Schott, F. (1999). The mean flow field of the tropical Atlantic Ocean. *Deep Sea Research Part II: Topical Studies in Oceanography*, *46*(1–2), 279–303. https://doi.org/10.1016/S0967-0645(98)00109-X

Tchamabi, C. C., Araujo, M., Silva, M., & Bourlès, B. (2017). A study of the Brazilian Fernando de Noronha island and Rocas atoll wakes in the tropical Atlantic. *Ocean Modelling*, *111*, 9–18. https://doi.org/10.1016/j.ocemod.2016.12.009

Thomas, L. N. (2005). Destruction of potential vorticity by winds. *Journal of Physical Oceanography*, *35*(12), 2457–2466. https://doi.org/10.1175/JPO2830.1

Van Sebille, E., Griffies, S. M., Abernathey, R., Adams, T. P., Berloff, P., Biastoch, A., et al. (2018). Lagrangian ocean analysis: Fundamentals and practices. *Ocean Modelling*, *121*, 49–75. https://doi.org/10.1016/j.ocemod.2017.11.008

Van Sebille, E., Zettler, E., Wienders, N., Amaral-Zettler, L., Elipot, S., & Lumpkin, R. (2021). Dispersion of surface drifters in the tropical Atlantic. *Frontiers in Marine Science*, *7*, 1243. https://doi.org/10.3389/fmars.2020.607426

Wenegrat, J. O., Thomas, L. N., Gula, J., & McWilliams, J. C. (2018). Effects of the submesoscale on the potential vorticity budget of ocean mode waters. *Journal of Physical Oceanography*, *48*(9), 2141–2165. https://doi.org/10.1175/jpo-d-17-0219.1

Whalen, C. B., de Lavergne, C., Garabato, A. C. N., Klymak, J. M., MacKinnon, J. A., & Sheen, K. L. (2020). Internal wave-driven mixing: Governing processes and consequences for climate. *Nature Reviews Earth & Environment*, *1*(11), 1–16. https://doi.org/10.1038/s43017-020-0097-z